Doctoral Dissertations

Graduate School

Spring 2003

A lateral comb drive on PMMA by hot embossing technique

Yongjun Zhao

Follow this and additional works at: https://digitalcommons.latech.edu/dissertations

A LATERAL COMB DRIVE ON PMMA BY

HOT EMBOSSING TECHNIQUE

By

Yongjun Zhao, B. E.

A Dissertation Presented in Partial Fulfillment of the
Requirement for the Degree of
Doctor of Philosophy in Engineering

COLLEGE OF ENGINEERING AND SCIENCE
LOUISIANA TECH UNIVERSITY

[May 2003]

LOUISIANA TECH UNIVERSITY

THE GRADUATE SCHOOL

<u>05/11/2003</u>

Date

     We hereby recommend that the thesis/dissertation prepared under our supervision

by   **Yongjun Zhao**

entitled   **A Lateral Comb Drive on PMMA by Hot Embossing Technique**

be accepted in partial fulfillment of the requirements for the Degree of

Doctor of Philosophy in Engineering

Supervisor of Dissertation Research
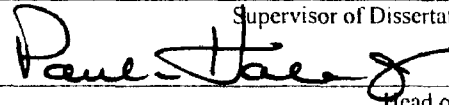
Head of Department

Electrical Engineering

Department

Recommendation concurred in:
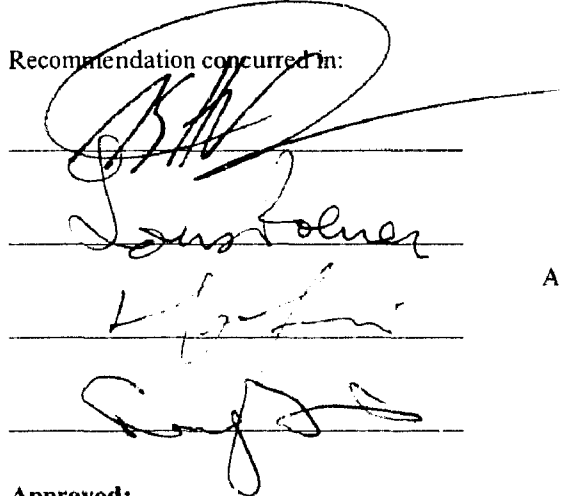
Advisory Committee

Approved:

Director of Graduate Studies

Approved:

Dean of the Graduate School

Dean of the College

ABSTRACT

The objective of this work is to fabricate a laterally driven comb drive on low-cost poly-methyl-meth-acrylate (PMMA) by hot embossing technology.

An electrostatic comb drive is one of the most important components in Micro-Electro-Mechanical Systems (MEMS). A comb drive can work as both a sensor and an actuator. Varieties of comb drives have been developed on silicon and poly-silicon materials.

Hot embossing of polymers is a promising alternative to traditional silicon processes due to cost-reduction. It fulfills the demand for low-cost methods for high volume production of micro-components and micro-systems. The raw materials of polymer are relatively unexpensive. For the manufacturing, a complex micromachining step for the fabrication of mold insert is only necessary once. The desired microstructures can be batch-replicated using the master mold.

In this work we used Finite Element Analysis software to design the structures. Several new process methods have been developed for achieving micro-mechanical structures with high aspect ratio on PMMA by hot embossing technique, forming mold insert by bonding a silicon-wafer mold onto a stainless steel disk, and releasing movable structures on PMMA material.

The comb drive microstructure, consisting of 80 units of interdigitated parallel capacitors with the finger gap and width of both 10 μm, has been fabricated successfully

under a typical condition of molding force of 35000 N at 135°C. The minimum feature size is 5 μm and the thickness of the structure is 60 μm, which makes the aspect ratio 12:1. The comb drive strokes 5 μm under a driven potential of 180 V. The natural frequency for the first mode of this comb drive is about 3 kHz.

The testing results matched the simulation results very well. Several advantages of this technique are observed as follows: (1) the whole process is simple and low cost, (2) all the processes are performed under low temperature, below 140°C, (3) PMMA structure has less stress and higher flexibility compared with the counterpart on silicon or poly-silicon, and (4) the driven voltage is much lower compared with the silicon-based devices.

The disadvantage of PMMA material is that it can not endure high temperature.

APPROVAL FOR SCHOLARLY DISSEMINATION

The author grants to the Prescott Memorial Library of Louisiana Tech University the right to reproduce, by appropriate methods, upon request, any or all portions of this Thesis/Dissertation. It is understood that "proper request" consists of the agreement, on the part of the requesting party, that said reproduction is for his personal use and that subsequent reproduction will not occur without written approval of the author of this Thesis/Dissertation. Further, any portions of the Thesis/Dissertation used in books, papers, and other works must be appropriately referenced to this Thesis/Dissertation.

Finally, the author of this Thesis/Dissertation reserves the right to publish freely, in the literature, at any time, any or all portions of this Thesis/Dissertation.

Author _____

Date _____

TABLE OF CONTENTS

LIST OF TABLES

LIST OF FIGURES

ACKNOWLEDGMENT

I would like to extend my sincere gratitude and appreciation to those who provided me with guidance and assistance in the preparation of this dissertation. Heartfelt thanks are extended to Dr. Tianhong Cui for serving as the major advisor on my graduate dissertation. His guidance and assistance in advice, time, and support will be forever remembered and appreciated. Special acknowledgements are extended to Dr. Kody Varahramyan, Dr. Frank Ji, Dr. Louis E. Roemer, and Mr. Ji Fang for serving as advisory committee members of this dissertation. Special thanks are extended to Dr. Yongjun Yang for valuable discussion on design and processes.

The author would like to thank the staffs at Institute For Micromanufacturing for their helps on the process performance.

Much gratitude is extended to my friends Jing Wang and Wei Xue for their valuable discussion, support, and contributions.

CHAPTER ONE

INTRODUCTION

1.1 Micromachined comb drive

An electrostatic comb drive is one of the most important components in Micro-Electro-Mechanical Systems (MEMS). A standard comb drive is formed by two sets of fingers with uniform gaps (Fig. 1.1). Each pair of fingers forms a parallel capacitor. One set of fingers is fixed on the substrate, which is called the fixed or stationary finger. The other set is free to move relatively to the fixed set, forming the moving finger. Moving fingers can move either laterally with the gaps fixed or vertically with the gaps closing to one side or the other.
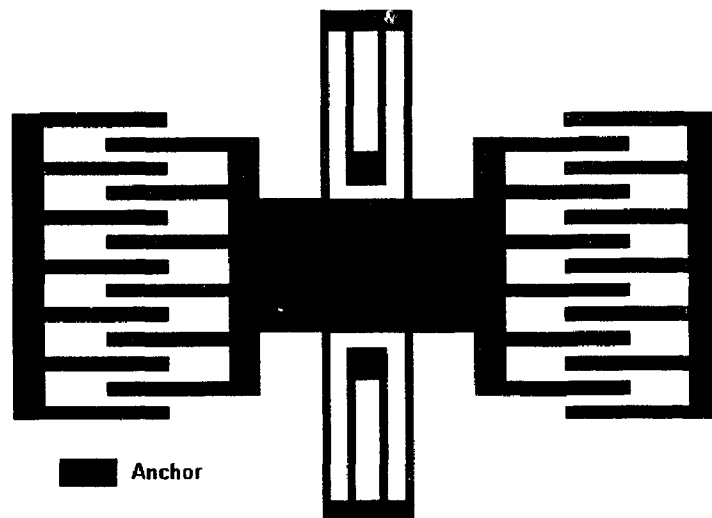
Figure 1.1   Schematic diagram of a standard comb drive
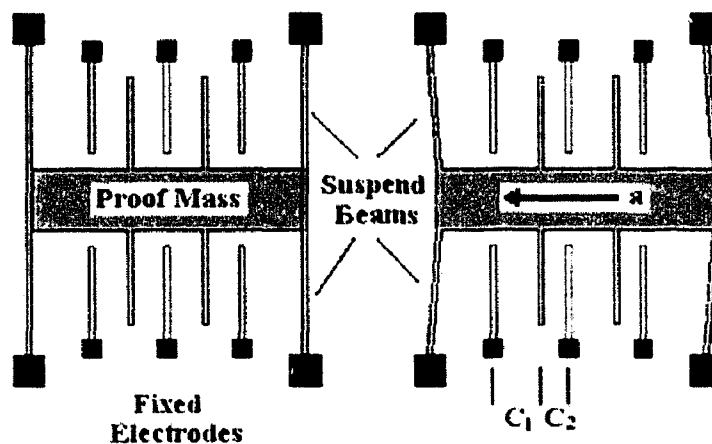
Figure 1.2   Top view of a laterally moved proof mass

A comb drive can work as a sensor and an actuator. For example, Fig. 1.2 shows the schematic diagram of the key part of a capacitance accelerometer. The acceleration is detected by the variation of the capacitance of capacitor C_1 and C_2 formed by a vertical driven comb drive. Thus, the comb drive works as capacitance sensor.

An example for a comb drive working as an actuator is illustrated in Fig. 1.3. Two sets of the comb drive working together change the tilt angle of the mirror panel through a set of gears so as to change the reflected direction of a laser beam.
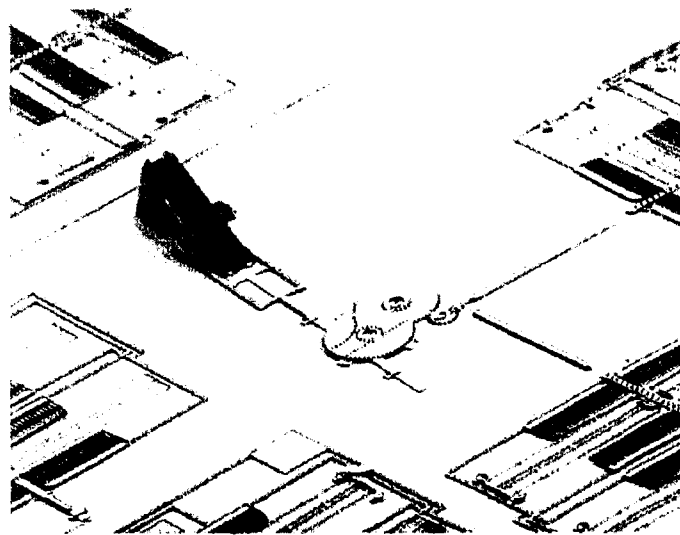
Figure 1.3   A comb drive working as an actuator[1]

1.2 Varieties of electrostatic comb drives

Much research and development on varieties of comb drives have been published since it was first presented by Tang, et al [2] [3]. William A. Johnson, et al. gave a thorough analysis on the physics in their paper of "Electrophysics of Micromechanical Comb Actuators" [4].

W. Ye, et al. presented an "optimal shape design of an electrostatic comb drives in microelectromechanical systems", in which the quadratic or cubic force profiles, beside the constant, and linear ones, under constant bias voltage by changing finger shape were given [5]. Their typical results are shown in Fig. 1.4.
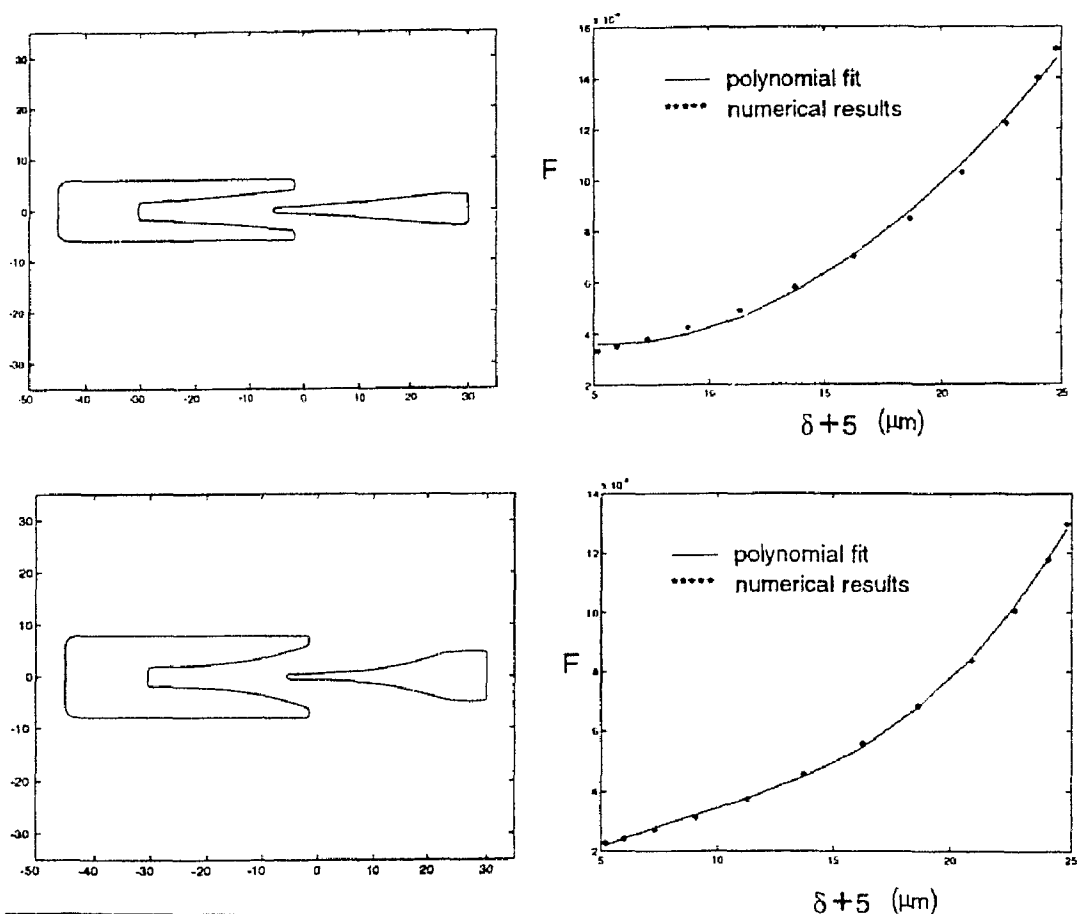
Figure 1.4   A comb drive with quadratic (upper) and cubic motion (lower)

M. Steven Rodgers, *et al.* presented an actuation system with a large force, low-voltage, and an efficient area (Fig. 1.5)[6]. An electrostatic shield is used to help reduce the distance between two sets of finger units closing to each other. Multiple-layer structures also efficiently reduce the area's size.
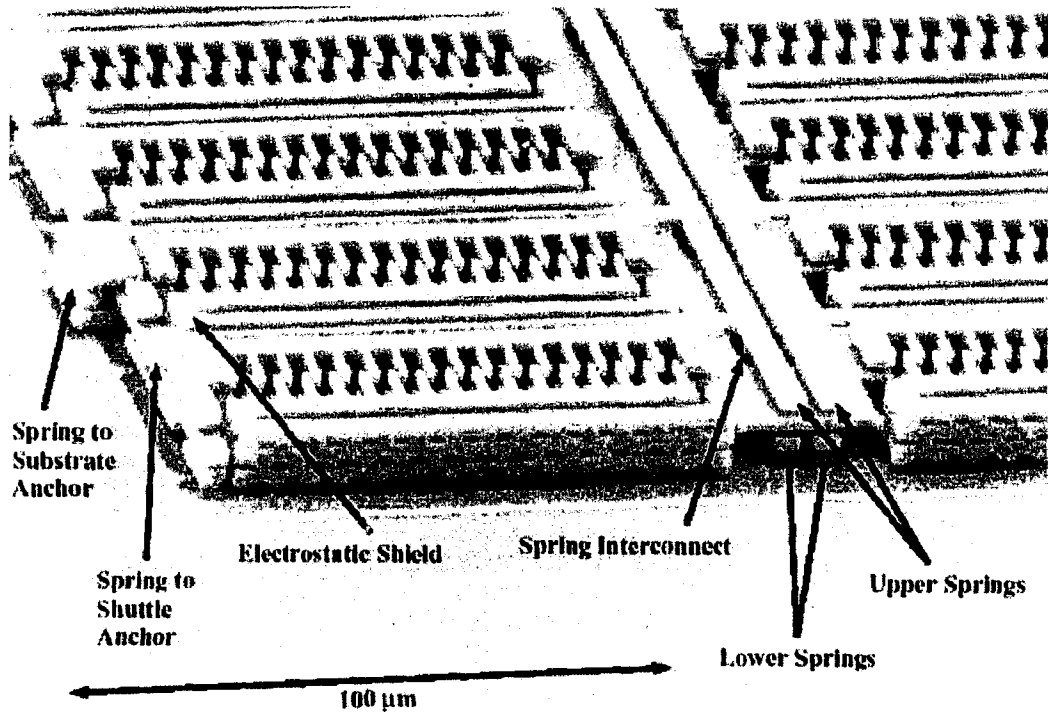
Figure 1.5   A comb drive with large force, low-voltage, and efficient area

J. L. Andrew *et al* reported an asymmetric comb drive in out-of-plane and torsional motions (Figure 1.6)[7]. Unlike an in-plane interdigitated comb drive, where the fingers of both combs are of the same thickness and in the same plane, the fingers on one comb of this asymmetric comb drive are thinner and higher than those on the other comb. The thin fingers will be pulled down toward the substrate when a voltage is applied betw en combs. The force imposed on the movable comb is shown in Fig. 1.6(b).

(a)   (b)
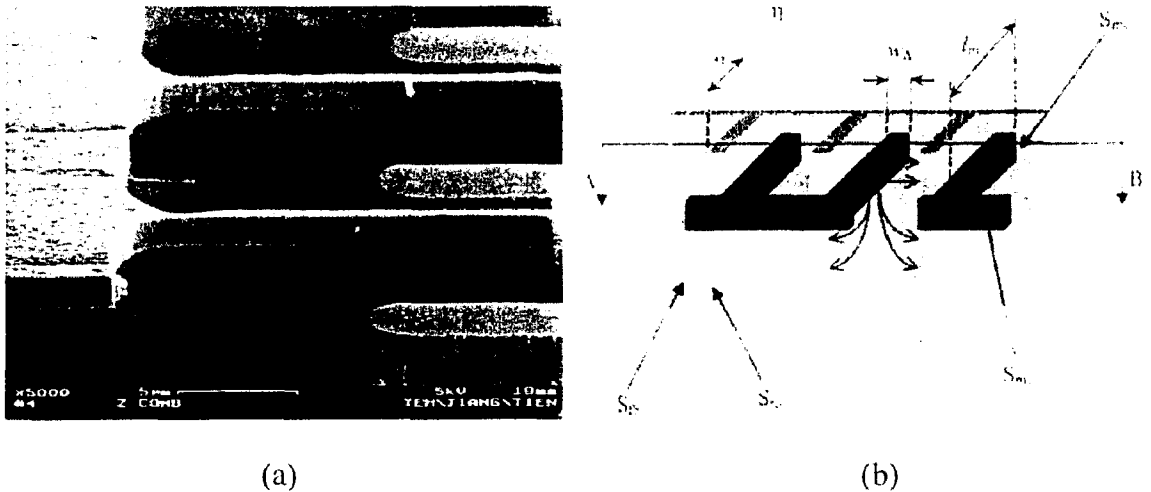
Figure 1.6   (a) A comb drive in out-of-plane motion; (b) Electric field force

Toshiki Hirano *et al.* reported a comb drive micro-actuator with sub-micron gaps on poly-silicon (Fig. 1.7) [8]. They used the so-called "oxidation machining" method to realize controlled submicron gaps. The basic idea is to make an electrode tooth with a certain width and to insert it into a gap whose width is slightly wider than that of the tooth. The shape of the electrode is made first by normal lithography and etching. After measuring the gap width, the size of the poly-Si electrode is shrank precisely so that the gap has the expected width. Oxidation of poly-Si followed by silicon dioxide removal is used to shrink the poly-Si so as to get controllable accuracy within 0.1 μm. The fabrication principle and procedures are shown in Fig 1.8. A three microns stroke under only about 10 V voltage is obtained with this submicron comb drive.

Figure 1.7 A comb drive with submicron gaps
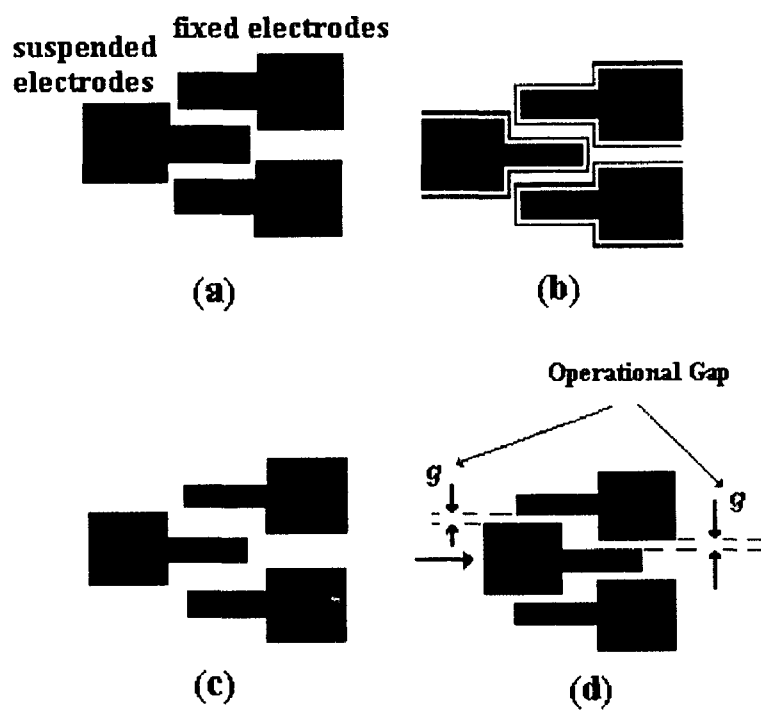
Figure 1.8 Schematic view of oxidation machining

An angular comb drive actuator was reported by Pamela R. Patterson *et al.* recently[9].

A novel angular vertical comb drive actuator was designed to drive a scanning mirror. A

resonant mode optical scan angle of ±18° at 1.4 kHz has been measured (Fig. 1.9).
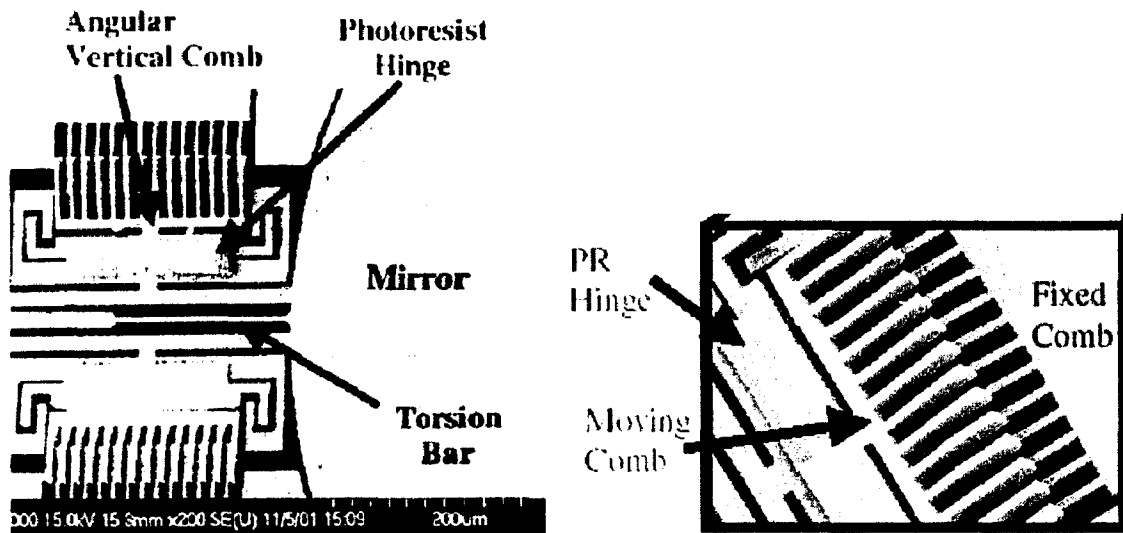
Figure 1.9   A mirror with angular vertical comb drive (left), enlarged comb (right)

1.3 Objective

Polymer materials are of great interest more and more in the Integrated Circuit (IC)

and MEMS research fields, and even industries as well, because they are relatively low

cost and easily processed. For instance, a 4-inch silicon wafer is normally more than $10.

A piece of poly-methyl-meth-acrylate (PMMA) the same size is only about $0.50.

Polymer materials are compatible with the traditional mass and batch IC processes very

well. Actually, some kinds of polymers, PMMA for instance, are used in IC industries all

the time.

In addition, polymer electronics and integrated circuits are rapidly growing research

fields at present. It is believed that polymer integrated circuits will take the place of

silicon integrated circuits on low-end applications in the future. This enables integration

of the mechanical structure of the polymer micro-sensors and electrical circuits onto a single polymer chip, eventually.

Hot embossing of polymers is a promising alternative to the traditional silicon processes for cost-reduction. It fulfills the demand for low-cost methods for high volume production of micro-components and micro systems. The raw materials of polymer are cheap. For the manufacturing, a complex micromachining step for the fabrication of mold insert is only necessary once. Then the desired microstructures can be batch replicated using the master mold. The overall process schematics of hot embossing is illustrated in Fig. 1.10.
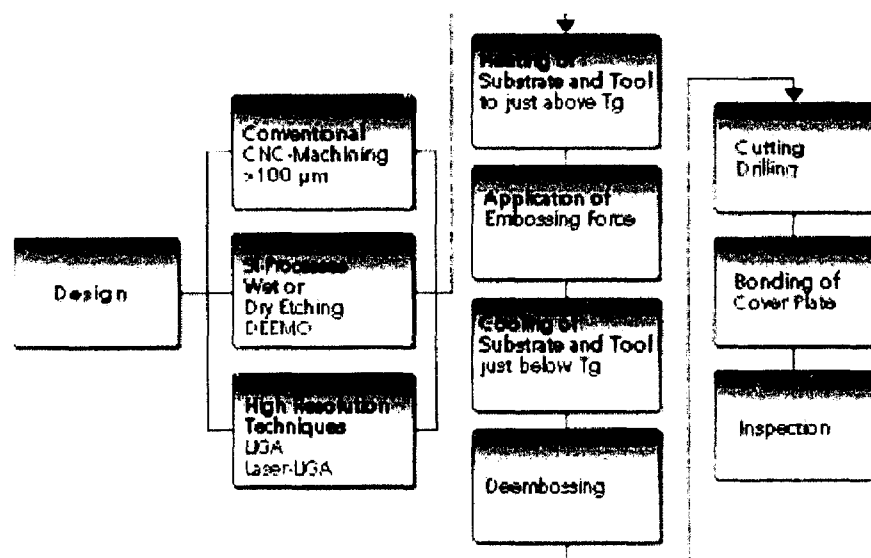
Figure 1.10 Process schematics of hot embossing[10]

This very novel technique is essentially the stamping of a pattern into a softened polymer by raising the polymer temperature above its glass transition temperature. It is an extremely precise and yet very simple process. It is also compatible with the conventional IC industry. It is mass and batch processes compatible as well due to the simple replication property. Homogeneity of materials, low internal stress and very thin

with high aspect ratio microstructures can be achieved by hot embossing process because it is a thermal equilibrium process.

During the last a few years hot embossing technology has been developed and applied to both laboratory and industry in broad fields. For example, Hot embossing lithography (HEL) has been proposed as one of the most promising methods to replace e-beam or x-ray lithography as the feature size is scaled down to nanometers for large area and mass production. In HEL a master mold could be made by e-beam lithography and proper etching processes. Next, the Nano-patterns are batch imprinted on the large-scale substrates by hot embossing [11,12,13]. Hot embossing has been well applied to the fabrication of micro fluidics devices on PMMA substrates for analytical chemistry and biomedical applications such as micro total analysis systems (u-TAS), *i.e.* the lab-on-a-chip [14][15]. As mentioned previously, polymer microfabrication by hot embossing is also becoming increasingly important as a low-cost alternative to silicon or glass-based MEMS technologies [16,17,18,19,20].

Thus, the objective of this research work is to achieve a comb drive structure on low cost polymer by the novel technology of hot embossing.

1.4 Methodology

The total concept map for the methodology is given in Fig. 1.11. An approximate goal of stroking 5 μm under 200 V potential bias with the first natural frequency of 3 KHz is set first. The next step in the design is to decide the spring constant and proof mass. Spring constant is decided by the suspension beam dimensions and structures. To make the first trial easier, double straight beams are used. The interdigitated fingers are put in the middle between the two beams. The schematic illustration of the structure is

shown in Fig. 1.12. The mass of proof mass is decided by the area and height of the

movable part.

```
                        ┌─────────────┐
                        │ Comb Drive  │
                        └─────────────┘
                               │
                               ▼
        ┌────────────────▶┌──────────────────────────┐◀─────────────┐
        │                 │ Beam/proof Mass Geometry  │              │
        │                 └──────────────────────────┘              │
        │                      │                    │                │
        │                      ▼                    ▼                │
        │              ┌─────────────┐      ┌────────────────┐       │
        │              │ Mask Layout │      │  Simulation    │───────┘
        │              └─────────────┘      │  FEA (ANSYS)   │◀──────┐
        │                      │            └────────────────┘       │
        │                      ▼                                     │
        │              ┌──────────────┐                              │
        │              │ Process Flow │                              │
        │              └──────────────┘                              │
        │                      │                                     │
        │         ┌────────┬───┴────┬─────────┬──────────┐           │
        │         ▼        ▼        ▼         ▼           │          │
        │   ┌─────────┬──────────┬─────────┬──────────┐   │          │
        │   │    1    │    2     │    3    │    4     │   │          │
        │   │  Mold   │Mold Insert│  Hot   │  Device  │   │          │
        │   │Fabrication│ Bonding │Embossing│Fabrication│  │          │
        │   └─────────┴──────────┴─────────┴──────────┘   │          │
        │         ▲        ▲        ▲         ▲           │          │
        │         └────────┴───┬────┴─────────┴───────────┘          │
        │                      ▼                                     │
        │              ┌──────────────┐                              │
        └──────────────│ Measurement  │◀─────────────────────────────┘
                       │  and Test    │
                       └──────────────┘
```
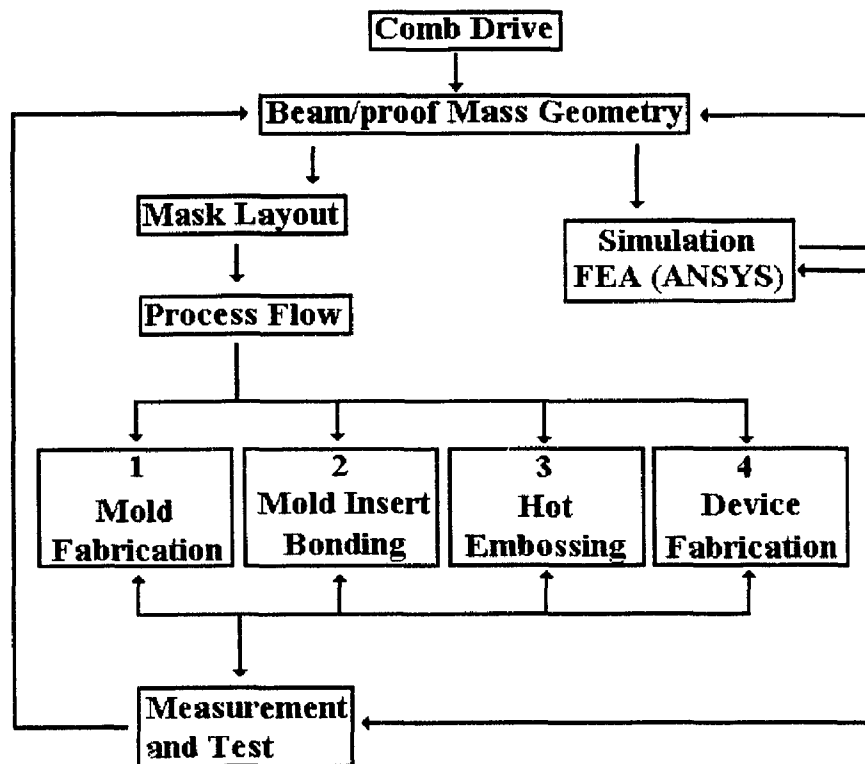
Figure 1.11 Concept map for the methodology

The spring constant and the natural frequency are mainly governed by the static and

dynamic mechanics. The deflection of the beams is governed by static mechanics. The

natural frequency, response time, and response reactions are governed by dynamic

mechanics when the comb drive is driven by an oscillatory force or by a shock force.

In the real practice of geometry design, simulation software is necessary to deal with

the complicated structures. Simulation software also makes it easier to modify and

optimize the design. Simulation can also help us to judge the experimental results and

estimate the process error.
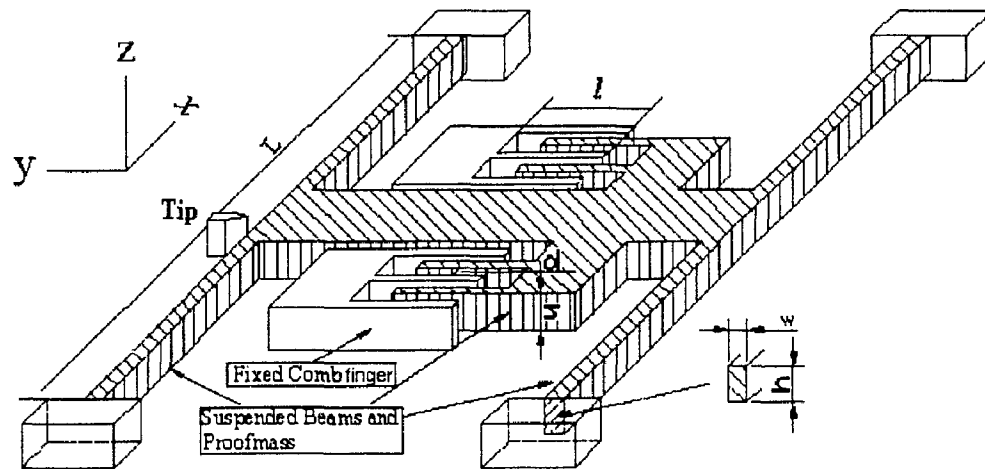
Figure 1.12 Schematic illustration of proposed comb drive

The mask layout was designed by assistance of the AutoCad software after the beam and proof mass geometry was decided. Of course, in this stage the process limitation factors should be taken into account. Then the process flow could be deployed. The initial measurement could be performed after the device is obtained. It is necessary to go back to the beam and proof mass geometry design again if the initial measurement results are far away from the goal. This process might need to be repeated several times until the final results are satisfied.

A fixed tip electrode is placed close to one suspension beam center. The gap between the tip and beam is 5 μm. This tip electrode serves two purposes. One is to measure the beam displacement. Once the beam touches the tip, an electrical signal on the tip electrode can be obtained, from which we can know that the beam has been displaced 5 μm. The other purpose of this tip electrode is to form a tunneling channel. This is our second objective for the next step beyond this work.

CHAPTER TWO

ANALYTICAL CALCULATIONS

2.1 The basic idea

The top view of the main structure is shown in Fig. 2.1. The hatched parts with lines are fixed on the substrate. The substrate is another PMMA sheet with spacers, which are formed using hot embossing process too. Proof mass (black part) is suspended by two suspension beams which are also part of proof mass. A fixed tip is placed 5 μm closing to the center of one suspension beam.
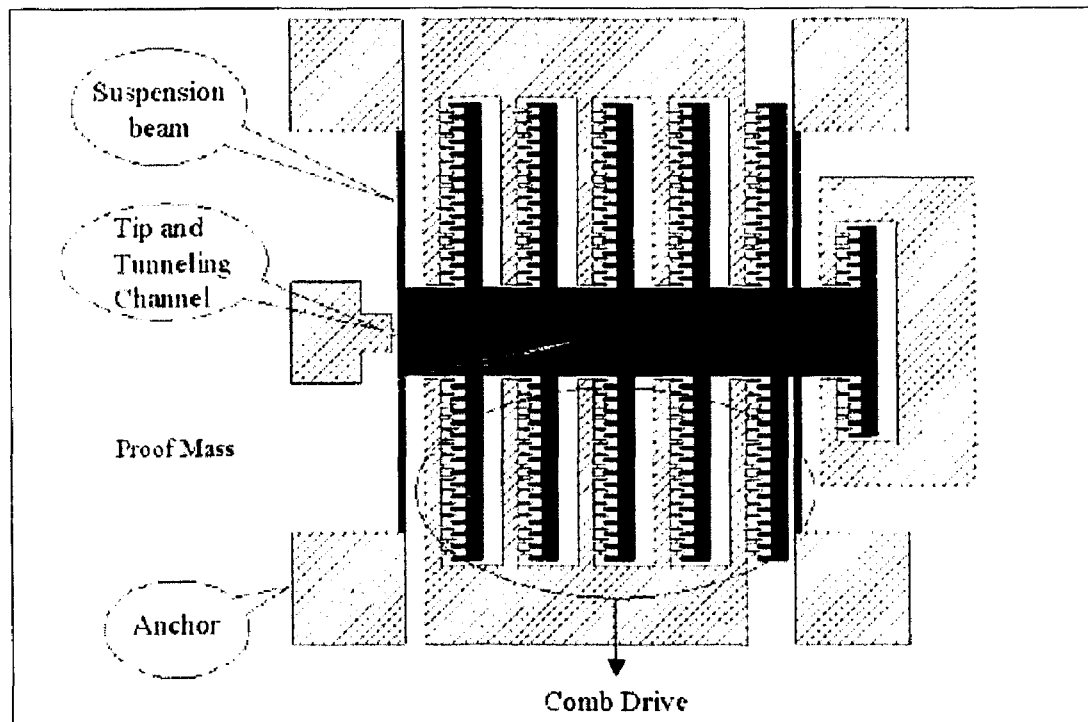
Figure 2.1 Overview sketch of the main structure

2.2 Second order mechanical system

The main body of the proposed comb drive can be modeled as a classical second order mechanical system with single degree-of-freedom. It is a damped mass-spring system under an applied force as shown in Fig. 2.2.
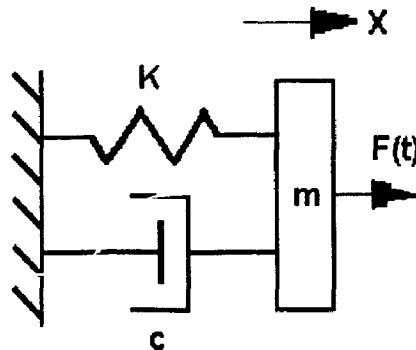
Figure 2.2   Single degree-of-freedom second order mechanical system

The motion is assumed to be only lateral. Here, m is the mass of proof-mass, k is the stiffness of the spring, i.e. the spring constant, x is the displacement of the mass from the equilibrium position and c is the damping coefficient. $F(t)$ is applied external force.

2.3.1 Equation of the motion

According to Newton's second law, the differential equation of the motion of forced second order mechanical system is given by:

$$m\frac{d^2x}{dt^2} = F(t) - kx - c\frac{dx}{dt}$$

(2-1)

where, t is time. Rearrange it:

$$\frac{m}{k}\frac{d^2x}{dt^2} + \frac{c}{k}\frac{dx}{dt} + x = \frac{1}{k}F(t)$$

(2-2)

2.3.2 Free vibration

Under free motion without external force, the differential equation becomes:

$$\frac{m}{k}\frac{d^2x}{dt^2} + \frac{c}{k}\frac{dx}{dt} + x = 0 \tag{2-3}$$

From mathematics, we know that the solutions of this linear differential equation with constant coefficients have an exponential form:

$$x = Ae^{rt} \tag{2-4}$$

Substituting (2-4) into (2-3) we have:

$$Ae^{rt}\left(\frac{m}{k}r^2 + \frac{c}{k}r + 1\right) = 0 \tag{2-5}$$

Then the so-called characteristic equation is obtained:

$$\frac{m}{k}r^2 + \frac{c}{k}r + 1 = 0 \tag{2-6}$$

Equation (2-6) has two roots:

$$r_{1,2} = \frac{1}{2}\left[-\frac{c}{m} \pm \sqrt{\left(\frac{c}{m}\right)^2 - \frac{4k}{m}}\right] \tag{2-7}$$

Hence, the solution of Equation (2-6) can be written as:

$$x = A_1 e^{r_1 t} + A_2 e^{r_2 t} \tag{2-8}$$

The natural resonant angular frequency (ω_n) and the damping ratio (ζ) can be defined as:

$$\omega_n = \sqrt{\frac{k}{m}} \tag{2-9}$$

$$\zeta = \frac{c}{c_c} \tag{2-10}$$

The critical damping coefficient (c_c) is defined by the vanishing of the discriminant in equation. (2-7):

$$\left(\frac{c_c}{m}\right)^2 - \frac{4k}{m} = 0 \tag{2-11}$$

Combining equations (2-11) and (2-9) yields:

$$c_c = 2\sqrt{km} = 2m\omega \tag{2-12}$$

Then from equation (2-10), we have:

$$c = 2m\zeta\omega \tag{2-13}$$

$$\zeta = \frac{c}{2\sqrt{km}} \tag{2-14}$$

Thus, equation (2-7) can be written as:

$$r_{1,2} = -\zeta\omega \pm \omega\sqrt{\zeta^2 - 1} \tag{2-15}$$

Therefore, the form of the solution depends on the value of the parameter ζ. There are three different solutions depending on ζ values.

I) Over-damped, $\zeta > 1$. Here, there are no oscillations. The proof mass just returns to equilibrium with at most one crossing through the equilibrium position on the way to equilibrium. This case is quite rare in practical mechanical systems. The solution is:

$$x = A_1 e^{-\zeta\omega t + \omega\sqrt{\zeta^2 - 1}t} + A_2 e^{-\zeta\omega t - \omega\sqrt{\zeta^2 - 1}t} \tag{2-16}$$

II) Critical damped, $\zeta = 1$. This case is seldom encountered in practical mechanical systems. In this case, the characteristic equation has a double root:

$$r_1 = r_2 = -\omega \tag{2-17}$$

The response solution is:

$$x = A_1 e^{-\omega t} + A_2 t e^{-\omega t} \tag{2-18}$$

III) Under-damped, $\zeta < 1$. This is the most important case in practical applications. In this case, the damping is small and oscillations persist forever, and the amplitude diminishes exponentially in time. In under-damped cases, the roots are conjugate complex numbers:

$$r_{1,2} = -\zeta\omega \pm j\omega\sqrt{1-\zeta^2} \qquad (2\text{-}19)$$

The general solution takes the following form:

$$x = A_1 e^{-\zeta\cdot\omega\cdot t + j\omega\sqrt{1-\zeta^2}\cdot t} + A_2 e^{-\zeta\cdot\omega\cdot t - j\omega\sqrt{1-\zeta^2}\cdot t} \qquad (2\text{-}20)$$

Or it can be written in more convenient form:

$$x = Ae^{-\zeta\cdot\omega\cdot t}\sin\left(\omega\sqrt{1-\zeta^2}\cdot t + \phi\right) = Ae^{-\zeta\cdot\omega\cdot t}\sin\left(\omega_d t + \phi\right) \qquad (2\text{-}21)$$

Where ω_d is the natural angular frequency of a damped system and ϕ is the phase angle:

$$\omega_d = \omega\sqrt{1-\zeta^2} \qquad (2\text{-}22)$$

Fig. 2.3 shows the solution of equation (2-3) with initial conditions $x = x_0$, $x' = 0$ for $t_0 = 0$ and with different damping ratios.

2.3.3 Harmonic excitation and response

A harmonic excitation is present if:

$$F(t) = F_0 \sin(\omega\cdot t) \qquad (2\text{-}23)$$

Where F_0 is the amplitude of the excitation force and ω is the angular frequency of the force. Using equation (2-2) yields:

$$\frac{m}{k}\frac{d^2x}{dt^2} + \frac{c}{k}\frac{dx}{dt} + x = \frac{1}{k}F_0 \sin(\omega\cdot t) \qquad (2\text{-}24)$$
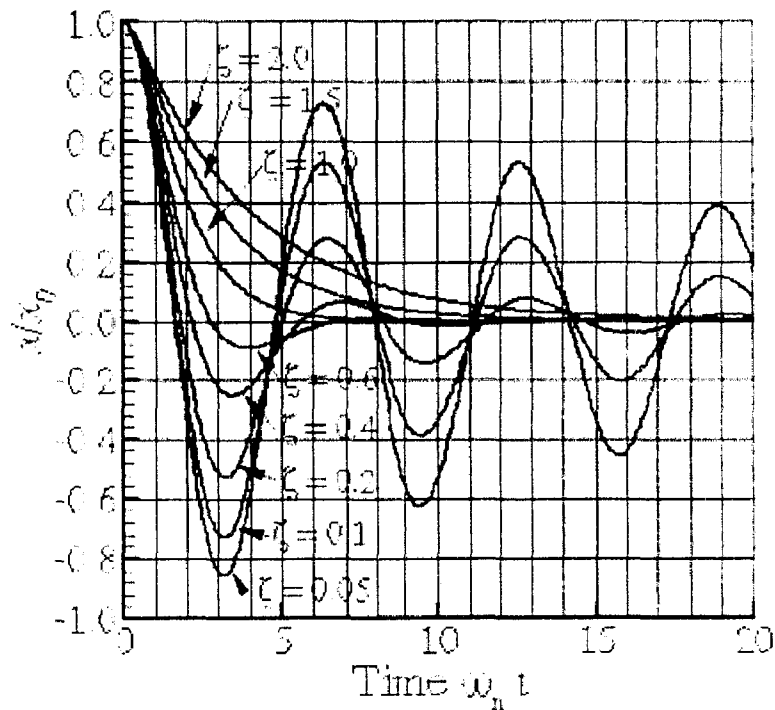
Figure 2.3   Free motion under different damping [21]

If we set:

$$\omega_n = \sqrt{\frac{k}{m}} \qquad \zeta = \frac{c}{2\sqrt{km}} \qquad K = \frac{1}{k}$$

Eq. (2-24) can be written as:

$$\frac{1}{\omega_n^2}\frac{d^2x}{dt^2} + \frac{2\zeta}{\omega_n}\frac{dx}{dt} + x = KF(t) \tag{2-25}$$

From mathematics we know that the solution has the form of:

$$x(t) = x_h(t) + x_p(t) \tag{2-26}$$

where, $x_h(t)$ is the transient solution (or homogeneous solution). One can see from

the results that for large time, the transient solution always decays to zero. $x_p(t)$ is the

steady state solution (or particular solution). The steady state solution should have a sinusoidal form also:

$$x_p(t) = X_0 \sin(\omega \cdot t + \phi) \tag{2-27}$$

Here X_0 is the amplitude of the response and ϕ is the phase angle. Substituting Eq. (2-27) into (2-25) gives:

$$X_0 = \frac{KF_0}{\sqrt{\left(1 - \omega^2/\omega_n^2\right)^2 + \left(2\zeta\omega/\omega_n\right)^2}} \tag{2-28}$$

$$\phi = \tan^{-1}\left(\frac{-2\zeta\omega/\omega_n}{1 - \omega^2/\omega_n^2}\right) \tag{2-29}$$

Fig. 2.4 and Fig. 2.5 show the plots of the solutions of equations 2-28 and 2-29
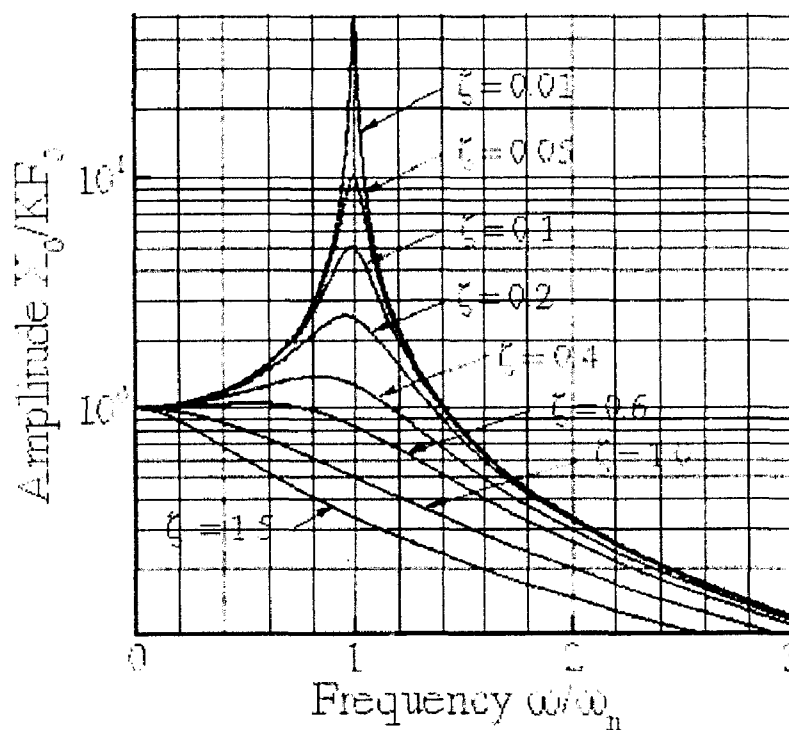
Figure 2.4   Steady state amplitude of vibration of a forced spring-mass system [21]
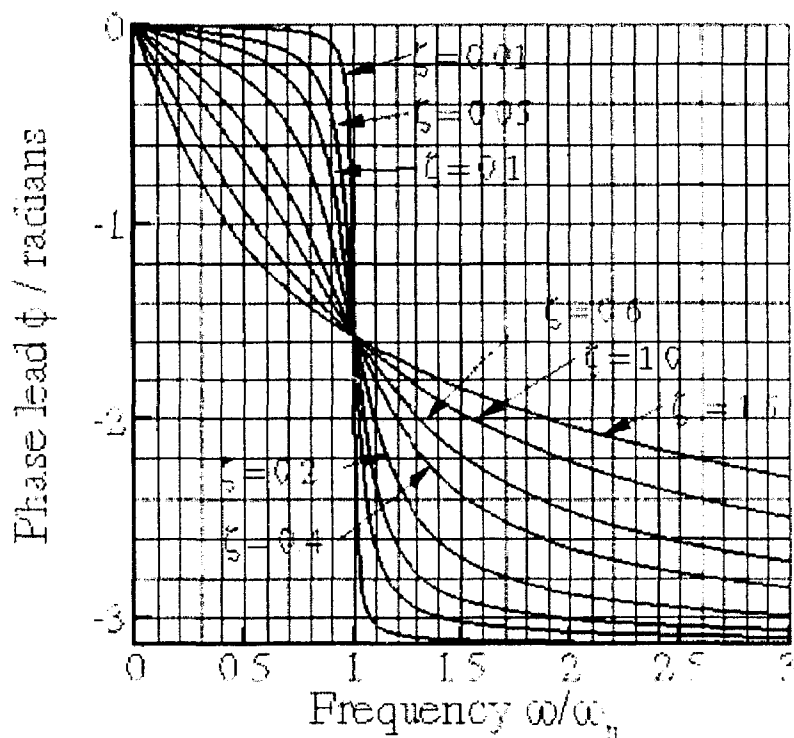
Figure 2.5 Steady state phase lead for a forced spring-mass system [21]

KF_0 is the displacement of the system subjected to a static force F ($KF_0 = F/k$). The frequency at which the amplitude is a maximum can be found by differentiating with respect to ω, setting the derivative equal to zero and solving the resulting equation for frequency. It turns out that the maximum amplitude occurs at a frequency

$$\frac{\omega}{\omega_n} = \sqrt{1 - 2\zeta^2}$$

This is the definition of the amplitude resonance. The corresponding value of X_0 is:

$$X_r = \frac{KF_0}{2\zeta\sqrt{1-\zeta^2}} \qquad (2\text{-}30)$$

In most practical cases, the damping is small, thus $\omega/\omega_n = \sqrt{1-2\zeta^2} \approx 1$. This is to say that the amplitude resonance occurs when the external exciting frequency approaches the system natural frequency, i.e. $\omega_{max} \approx \omega_n$.

2.3.4 Steady and transient response to forced vibrations.

The "steady state" response is defined as the behavior of the system when time gets very large. It is independent of the initial position and velocity of the mass. The behavior of the system while it is approaching the steady state is called the "transient" response. The transient response depends on everything.

If the damping coefficient is very small, the system takes longer to reach a steady state. Thus, the length of time to reach a steady state depends on the properties of the system and also the initial conditions.

That the system always settles to a steady state has two important consequences. Firstly, the initial conditions for a real engineering system are rarely known. Now one knows this doesn't matter – the response is not sensitive to the initial conditions. Secondly, if the transient response is not interested, the solutions to equations of motion can be greatly simplified. Thus, when analyzing forced vibrations, one (almost) always neglects the transient response of the system, and calculates only the steady state behavior.

In a summary

- The steady state response is always harmonic, and has the same frequency as that of the forcing.

- The amplitude of vibration is strongly dependent on the frequency of excitation, and on the properties of the spring-mass system.

- If the forcing frequency is close to the natural frequency of the system, and the system is lightly damped, huge vibration amplitudes may occur. This phenomenon is known as resonance.

- There is a phase lag between the forcing and the system response, which depends on the frequency of excitation and the properties of the spring-mass system.

2.3.5 Bandwidth and quality factor
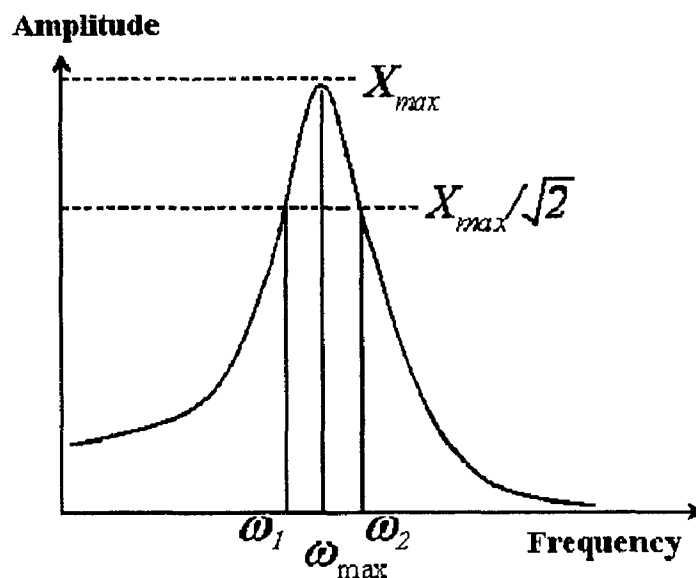
Figure 2.6   Plot of response amplitude vs excitation frequency.

Fig. 2.4 is re-plotted with absolute values instead of ratios in Fig. 2.6. In the plot, the maximum response X_{max} is corresponding to ω_{max}. If a horizontal line is drawn at amplitude $X_{max}/\sqrt{2}$, it will intersect with the response curve at frequency ω_1 and ω_2. The bandwidth of the response is defined as: $\Delta\omega = \omega_1 - \omega_2$. Because the energy dissipated at these frequencies is half of the energy dissipated at resonance this bandwidth is sometimes called the half-power bandwidth.

As mentioned previously, in most practical systems, the damping ratio is very small. Then, Eq. (2-30) can be written as:

$$X_r = \frac{KF_0}{2\zeta} = KF_0 Q \qquad (2\text{-}31)$$

where, Q is the so-called quality factor. Quality factor Q is also defined as:

$$Q = 2\pi \frac{W}{\Delta W} \qquad (2\text{-}32)$$

where, W is the energy stored in a system and ΔW is the energy dissipated per cycle.

According to the definition, as damping ration is small, we have:

$$X(\omega_1) = X(\omega_2) = \frac{X_{max}}{\sqrt{2}} \approx \frac{KF_0}{2\zeta\sqrt{2}} \qquad (2\text{-}33)$$

ω_1 and ω_2 must be solutions of the equation. Using Eq. (2-28) and (2-33) we can write the following equation for which ω_1 and ω_2 should be solutions:

$$\frac{KF_0}{2\zeta\sqrt{2}} = \frac{KF_0}{\sqrt{\left(1 - \omega^2/\omega_n^2\right)^2 + \left(2\zeta\omega/\omega_n\right)^2}} \qquad (2\text{-}34)$$

Solve this equation we get:

$$\left(\frac{\omega_1}{\omega_n}\right)^2 = \frac{2 - 4\zeta^2 - 4\zeta\sqrt{\zeta^2 + 1}}{2} \qquad (2\text{-}35)$$

$$\left(\frac{\omega_2}{\omega_n}\right)^2 = \frac{2 - 4\zeta^2 + 4\zeta\sqrt{\zeta^2 + 1}}{2} \qquad (2\text{-}36)$$

Subtract Eq. (2-35) from Eq. (2-36):

$$\left(\frac{\omega_2}{\omega_n}\right)^2 - \left(\frac{\omega_1}{\omega_n}\right)^2 = 4\zeta\sqrt{\zeta^2 + 1} \approx 4\zeta \qquad (2\text{-}37)$$

Rearranging it we have:

$$\left(\frac{\omega_2}{\omega_n}\right)^2 - \left(\frac{\omega_1}{\omega_n}\right)^2 = \frac{\omega_2 - \omega_1}{\omega_n} \cdot \frac{\omega_2 + \omega_1}{\omega_n} = \frac{\Delta\omega \cdot 2\omega_n}{\omega_n^2} \qquad (2\text{-}38)$$

Comparing the right side of Eq. (2-37) and (2-38):

$$\frac{\Delta\omega}{\omega_n} = 2\zeta = \frac{1}{Q} \qquad (2\text{-}39)$$

As we can see, quality factor also describes the sharpness of the resonance peak, the larger Q the narrower bandwidth. This equation also provides us with the common method to measure Q or damping ratio by measuring the resonant frequency and bandwidth.

2.4 Spring Constant

2.4.1 Deflection of beam

One of the most important parameters is the spring constant K. In our case it should be the spring constant of the two suspension beams. In order to know its spring constant we need to know the relationship between the deflection and loading force. The most common method to get this relationship involves the Euler-Bernoulli equation:

$$y(x) = -\frac{1}{EI} \iint M(x)dxdx + Cx + D \qquad (2\text{-}40)$$

where,

$x =$ direction along the neutral axis.

$y =$ direction along the transverse axis.

$E =$ Young's modulus.

$I =$ area moment of inertia.

$M(x) =$ the bending moment in the beam, which is usually a function of x.

$C, D =$ constants decided by boundary conditions.

In our specific case, analysis of one beam is performed first. It is a both-end-fixed cuboid beam. A uniformly distributed load is applied on the center.

The analysis process is shown below:
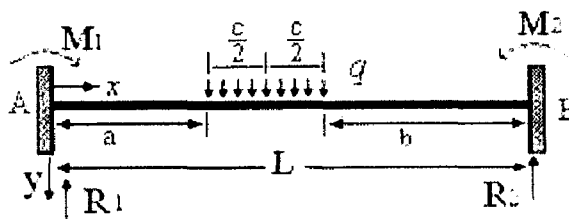
Figure 2.7 A two-end fixed beam with uniform loading in the middle

where,

$a = b;$ $a + c/2 = L/2;$ and $a <= x <= a + c$

M_1, M_2 are moments

R_1, R_2 are reaction forces

L is the beam length

The loading condition is illustrated in Fig. 2.7. A uniformly distributed loading with density q is applied in the middle. From common knowledge, we know that the maximum deflection will be at the center. Thus, the deflection from a to $a+c$ is mainly concerned. At the point $x = L/2$, the spring constant is:

$$K\left(\tfrac{L}{2}\right) = \frac{F}{y\left(\tfrac{L}{2}\right)} = \frac{qc}{\left(\tfrac{L}{2}\right)} \qquad (2-41)$$

Using the superposition method, this problem can be treated as three subdivided loadings applied on the one-end-fixed cantilever bear in the same time. And the deflections produced by these three subdivide loadings are known. If we assume that this two-end-fixed beam is fixed at A with end B free. Then, the three subdivided loadings

will be. a) The original loading with density q. b) The bending moment applied on point B which equals:

$$M_1 = M_2 = -\frac{qc}{12L^2}(12ab^2 + 6b^2c + 4ac^2 + 12abc + 4bc^2 + c^3) \qquad (2\text{-}42)$$

c) The concentrated loading applied on point B with force R which equals:

$$R_2 = R_1 = \frac{qc(a+c/2)}{L} + \frac{M_1 - M_2}{L} = \frac{qc}{2} \qquad (2\text{-}43)$$

We can find the solutions of the deflation on a cantilever with these three kinds of loading conditions directly from a mechanics textbook. For the loading q, we have:

$$y_c = \frac{q}{24EI}\left[x^4 + 4(a-L)x^3 + 6(L^2 - aL - a^2ac)x^2 - 4a^3x + a^4\right] \qquad (2\text{-}44)$$

For the loading of bending moment:

$$y_M = \frac{qc}{24EIL^2}\left(12a^3 + 18a^2c + 8ac^2 + c^3\right)x^2 \qquad (2\text{-}45)$$

For the loading R

$$y_R = \frac{qc}{12EI}\left(x^3 - 3Lx^2\right) \qquad (2\text{-}46)$$

Then the final total deflection is

$$y = y_c + y_M + y_R \qquad (2\text{-}47)$$

At the middle point $x = L/2$, from Eq (2-47) we can get:

$$y\left(\tfrac{L}{2}\right) = \frac{q}{384EI}\left(48a^3c + 72a^2c^2 + 32ac^3 + 4c^4 - 20L^3c - 24acL^2 \right.$$
$$\left. + 17L^4 - 16aL^3 - 24a^2L^2 - 32a^3L + 16a^4\right) \qquad (2\text{-}48)$$

It is a very complicated expression. If c is small compared with L, for example $c \leq L/10$, it can be approximately simplified as a concentrated load in the middle with force of $F = qc$, which is true in our structure. Then Eq. (2-48) can be simplified as:

$$y = \frac{Fx^2(3L - 4x)}{48EI} \qquad (2\text{-}49)$$

And

$$y\left(\tfrac{L}{2}\right) = y_{max} = \frac{FL^3}{192EI} \qquad (2\text{-}50)$$

With the beam dimension as shown in Fig. 2.8 below, the area moment of inertia I equals:

$$I = \frac{hw^3}{12} \qquad (2\text{-}51)$$
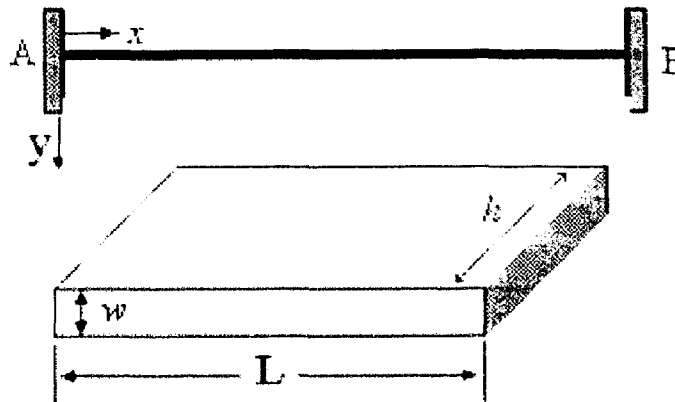
Figure 2.8 Sketch of a beam dimension.

where, w is the height and h is the width.

Then Eq. (2-50) will be:

$$y\left(\tfrac{L}{2}\right) = y_{max} = \frac{FL^3}{16Ehw^3} \qquad (2\text{-}52)$$

Now we can get the spring constant:

$$K = \frac{F}{y\left(\tfrac{L}{2}\right)} = \frac{16Ehw^3}{L^3} \qquad (2\text{-}53)$$

For two beams connected by a rigid bar in the center, the total spring constant is approximately double that of one beam when the width of the rigid bar is very small compared to the beam length. Then we have:

$$K = \frac{F}{y\left(\frac{L}{2}\right)} = \frac{32Ehw^3}{L^3}$$
(2-54)

However, in reality, the rigid bar will increase the total stiffness of this two beam system. The real total spring constant will be larger than the value expressed by the Eq. (2-54). The analytical solution will be more complicated for the total system. Fortunately, there are many commercial softwares, such as Finite Element Analysis (FEA) software ANSYS, which can solve this kind of problem easily. In this research work, we use the approximate analytical calculation for the initial dimension trial then use ANSYS FEA software to optimize the spring constant precisely.

2.5 Electrostatic comb drive

Normally, a laterally moving comb drive works as an electrostatic actuator. In this way, it can give a constant force and has a large stroke distance. Gap-closing combs often work as a capacitive sensor. In this way, the capacitance variation is approximately inversely proportional to the square of gap distance. In our device we use the lateral comb drive. The lateral comb drive is mainly discussed in the following chapter.

2.5.1 Electrostatic force for laterally driven

Considering one unit of the comb drive, as shown in Fig. 2.9, the energy stored in the capacitor is given by:

$$U_{e.l} = \frac{1}{2}CV^2 + \frac{1}{2}C''V^2$$

$$= \frac{1}{2}\left(\varepsilon\frac{hx}{g} + \varepsilon\frac{hx}{g'}\right)V^2 = \varepsilon\frac{hx}{g}V^2$$

(2-55)

where,

$g=g'$ in this case.

V is the potential voltage between the fixed and moving fingers.

ε is the permittivity of the medium surrounding the fingers, normally air.
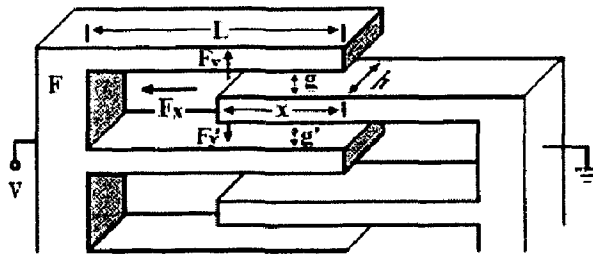
Figure 2.9   The sketch of a standard comb drive

Then the driving force acting on the moving finger is:

$$F_{x,y} = -\frac{\partial U_{e.l}}{\partial x} = -\frac{\varepsilon h}{g}V^2$$

(2-56)

It is a constant force because the changing rate of capacitance is constant. Moreover, larger stroke displacement can be obtained in this case. However, the force is normally small. For a comb drive consisted by n units, the driving force would be

$$F_{Total} = -\frac{n\varepsilon h}{g}V^2$$

(2-57)

2.5.2 Considerations in designing a
lateral comb drive

2.5.2.1 Gap-closing driven force and pull-in problems: In a comb drive there is not

only the laterally driven force but also gap-closing driven force (y direction moving in

Fig. 2.9). The driven force is:

$$F_{y,i} = F_y - F_{y'} = \frac{-\partial U_{c,i}}{\partial g} - \frac{-\partial U'_{c,i}}{\partial g'} = \frac{1}{2}\frac{\varepsilon h x}{g^2}V^2 - \frac{1}{2}\frac{\varepsilon h x}{g'^2}V^2 \approx \frac{1}{2}\frac{\varepsilon h x}{g^2}V^2 \quad (2\text{-}58)$$

Because the gap distance is normally smaller relative to the height and overlap length,

a gap-closing driven comb drive has a larger force than a laterally driven drive. It is a

nonlinear force under constant bias voltage. For a comb drive consisting by n units, the

driving force would be

$$F_{Total} = \frac{n\varepsilon h x}{2g^2}V^2 \quad\quad\quad (2\text{-}59)$$

If the moving fingers remain precisely at the centers between the fixed fingers, the

gap-closing driving force is canceled. However, the gap-closing driving force at the end

fingers cannot be canceled. Therefore, if the voltage is high enough or the end fingers are

thin enough, the fingers will bend significantly. In the extreme case, the fingers will

clamp together, resulting in a circuit short and failure. This problem is especially

significant on polymer structures because the Young's modulus of most polymers used in

hot embossing processes is only 2~3 x 10^9.

The direct evaluation of the relationship between voltage and bending is difficult

because it is a coupled multiple physical field. The attractive force from the electrostatic

field results in the bending of the finger. In turn, the bended finger results in the increase

of the electrostatic force, which will again result in further finger bending until the

restoring elastic force of the finger balances the electrostatic force. In our practice, ANSYS 5.7 from the ANSYS Company (http://www.ansys.com) is used to solve this problem. The simulation process is explained in detail in the following chapter 3.

The simplest and best way to prevent the end fingers from pull-in is to increase their thickness. From basic mechanical theory, the displacement of a one-end fixed beam is given by:

$$\left. \begin{array}{r} D \propto k \dfrac{F}{EI} \\[2mm] I = \dfrac{ht^3}{12} \end{array} \right\} \Rightarrow D \propto k' t^{-3} \qquad\qquad (2\text{-}60)$$

where,

D - Displacement

F - Force

E - Young's modulus

I - Bending moment

h - Finger height

t - Finger thickness

k - Constant

From the above equations, we can see that the displacement is inversely proportional to the cube of the thickness.

2.5.2.2 The constant force: One of the most important features of lateral comb drive is that a constant driving force with a large stroke distance can be obtained under constant bias voltage. This linear relationship gives us many benefits to design varieties of micro sensors or actuators. However, when the moving fingers move close to the support beam of the fixed fingers, this constant force feature is no longer sustained. Now the

capacitance between the cross section of the moving finger and inside wall of the support beam of the fixed finger is significant. This relationship is investigated by using ANSYS, too. The detail process is discussed in chapter 3.

It has been observed that for a comb drive with the same gap distance and finger width of g, it enters the linear region from overlap length $2g$. The linear region stops at $3g$ before the finger ends approach to the inside surfaces of the support beams.

2.5.2.3 Stability: A comb drive is an inherently unstable system. As mentioned previously, there is substantial vertical driven force among the fingers. If the moving fingers remain precisely at the centers between the fixed fingers, the gap-closing driving force is canceled. However, any perturbation of the center fingers will cause an offset of the force and pull the fingers to one side or the other.
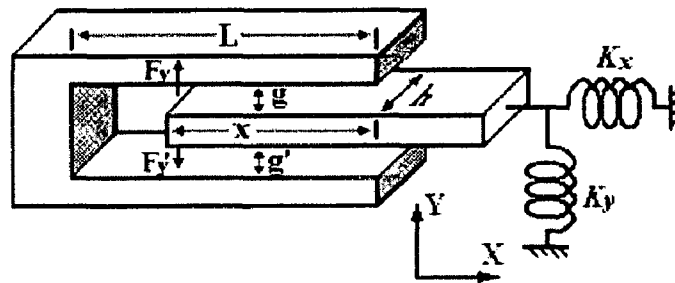
Figure 2.10 Sketch of a unit comb drive with mechanical springs

To consider the stability of the comb drive, we can "model" the electrostatic force as a virtual spring as illustrated in Fig. 10 [22]. Then the imaged spring constant should be given by

$$K_{image} = \frac{\partial F_y}{\partial y} \tag{2-61}$$

We have known that

$$F_y = \frac{\varepsilon h x V^2}{2(g-y)^2} - \frac{\varepsilon h x V^2}{2(g+y)^2} \qquad (2\text{-}62)$$

So this virtual spring has a imaged constant at $y=0$ of

$$K_{image} = \frac{\partial F_y}{\partial y}\bigg|_{y=0} = \frac{2\varepsilon h x V^2}{g^3} \qquad (2\text{-}63)$$

Then a comb drive is stable if the mechanical spring constant K_y, as indicated in Fig. 2.10, of the suspension of the moving fingers is much larger than this imaged spring constant K_{image}.

In engineering terms, the stability of a comb drive can also be considered in the way of energy storage. The key point to design a stable comb drive is to make sure that the energy stored in the x direction is much more than that in the y direction, i.e. $Ux \gg Uy$.

$$U_y = \frac{1}{2} K_y g^2 \qquad (2\text{-}64)$$

and

$$U_x = \frac{1}{2} K_x g^2 \qquad (2\text{-}65)$$

Thus, we have

$$K_y \ll \frac{x^2 K_x}{g^2} \qquad (2\text{-}66)$$

We can see that the structure should be much more rigid in the y direction than that in the x direction. However, satisfying the above deduced value of K_y will not guarantee the comb drive is stable enough for practice applications. A large safety factor should be put in a design.

2.6 Quality factor Q analysis

In 2.3.5 we discussed quality factor Q. Q is directly related to the damping coefficient ζ. From Eq. (2-39) we know that in a small damping system:

$$\zeta = \frac{1}{2Q}$$

(2-67)

Except for the response amplitude described in Eq. (2-28) and Fig. 2.4, damping coefficient ζ also influences many other parameters such as:

Displacement resonant frequency, $\omega_d = \omega_n \sqrt{(1 - 2\zeta^2)}$ (2-68)

Acceleration resonant frequency, $\omega_a = \dfrac{\omega_n}{\sqrt{(1 - 2\zeta^2)}}$ (2-68)

Damped natural frequency, $\omega_d = \omega_n \sqrt{(1 - \zeta^2)}$ (2-70)

Where ω_n is undamped natural frequency.

2.6.1 Squeeze-film damping

The main damping mechanism for microstructures operated at atmospheric pressure is often dominated by viscous air damping. Squeeze-film damping, illustrated in Fig. 2.11, is a typical viscous air damping. It arises from vertical motion of the plate in Fig. 2.11. When the plate moves toward the substrate a pressure in the thin film of air will be increased. This increased pressure consequently produces a resistant force, F, which is proportional to the velocity. In the meantime the air will be pumped out and into the thin film gap. The interaction between air molecules and the plate and among molecules themselves results in the energy dissipation.
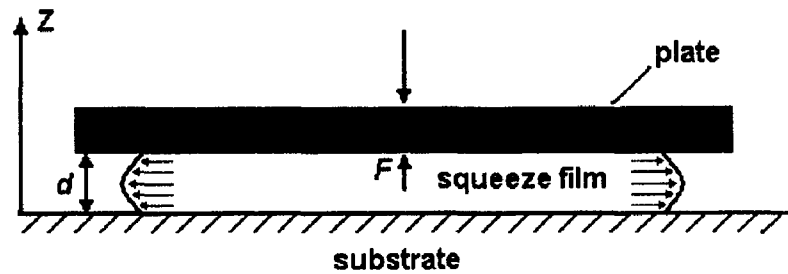
Figure 2.11 Cross-section sketch of a plate with an air gap

Continuum fluid mechanics can be used to analyze squeeze-film damping if the air gap is much larger than the mean-free-path, λ, of the air molecules. The mean-free-path of a gas is expressed as

$$\lambda = \frac{1}{\sqrt{2}\pi d_0^2 n}$$

(2-71)

where, πd_0^2 is the collision cross-section of the gas molecules. n is the molecular density, which, for an ideal gas, is given by

$$n = \frac{P}{K_B T}$$

(2-72)

Where P is pressure of the squeeze film, k_B is Batsman's constant, and T is absolute temperature. For air at atmospheric pressure and $T=300K$, the mean-free-path is about 65 nm. The minimum feature size in our structure is 5 μm which is much larger than the mean-free-path, thus the air can be modeled approximately as a viscous fluid.

With several assumptions, viscous-flow regime can be described with Navier-Stokes equation [23]:

$$\frac{\partial^2 P}{\partial x^2} + \frac{\partial^2 P}{\partial y^2} = \frac{12\mu}{d^3}\frac{\partial(\Delta d)}{\partial t}$$

(2-73)

Where P is pressure of the squeeze film, μ is the viscosity of air (1.8×10^{-5} Pa-s), d is the air-gap height, and Δd is the plate displacement. Eq. (2-73) requires that the squeeze film is isothermal and has small pressure variations, and that the plate undergoes small displacements with small velocities.

Air velocity in the gap can be considered small if the Reynolds number, Re, is much less than 1, where

$$R_e = \frac{dv\rho}{\mu} < 1 \qquad (2\text{-}74)$$

where, ρ is the density of air ($1.22\ Kg/m^3$), and v is the air velocity.

When the plate length in y-direction, Ly, is much larger than the length in the x-direction, Lx, as illustrated in Fig. 2.12, we can simplify the problem as one-dimensional approximation analysis. The drawing is not to scale. Eq. (2-73) then can be simplified to Eq. (2-75)

$$\frac{\partial^2 P}{\partial x^2} = \frac{12\mu}{d^3}v \qquad (2\text{-}75)$$

Double integration of Eq. (2-75) and application of the pressure boundary conditions at the edges of the plate gives

$$\Delta P = \frac{6\mu v}{d^3}\left(x^2 - \frac{L_x^2}{4}\right) \qquad (2\text{-}76)$$

where, ΔP is the pressure difference from ambient pressure. The average pressure difference across the plate is

$$\mu L_x^2 v / d^3$$
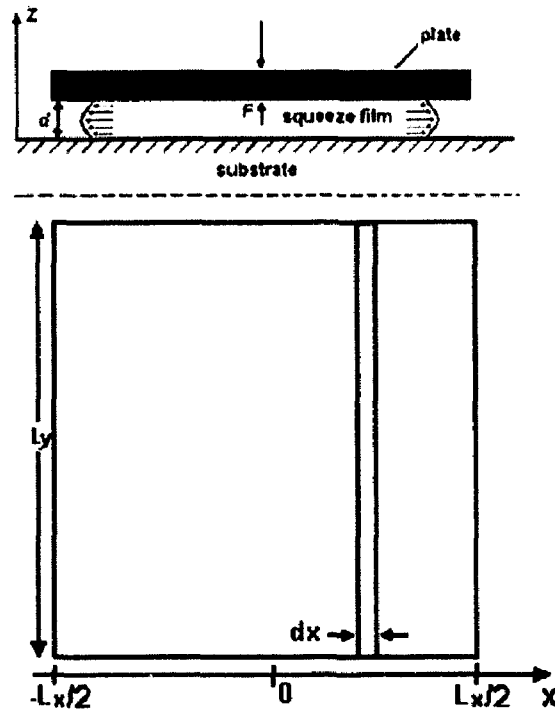
Figure 2.12 Sketch for one-dimensional analysis of squeeze-film damping

And the total force from damping exerted on the plate is:

$$F = -\left(\frac{\mu L_y L_x^3}{d^3}\right)v \tag{2-77}$$

Then the damping factor is

$$\frac{\mu L_y L_x^3}{d^3}$$

The squeeze-film damping factor for a rectangular plate is

$$D_s = K_{B_z}(L_x/L_y)\left(\frac{\mu L_y L_x^3}{d^3}\right) \tag{2-78}$$

Where $K_{B_z}(L_x/L_y)$ is a form factor that is introduced to account for the finite plate length, L_y. For a very long plate $(L_y >> L_x)$, we can deduce from Eq. (2-77) that $K_{B_z}=1$.

2.6.2 Laterally oscillating viscous damping

In addition to the squeeze-film damping there is also a laterally oscillating viscous damping which results from the relatively parallel movement of the surrounding air in respect to the moving plate. Young-Ho Cho, et al, gave out the detailed discussion on lateral damping in reference [24]. They compared two kinds of models, Couette-type and Stokes-type, and compared their results to the experiment measurement values.

Under the lateral oscillation of the plate, the ambient air-film is also governed by the Navier-Stokes equations. For a small-amplitude motion under no overall pressure gradient, the Navier-Stokes equations can be reduced to a one-dimensional diffusion equation:

$$\frac{\partial u}{\partial t} = v \frac{\partial^2 u}{\partial y^2}$$

(2-79)

where, v is kinetic viscosity, and

$$v = \mu / \rho$$

(2-80)

where, μ is absolute viscosity.

According to Newton's law of viscosity, the frictional shear, τ_0, on the plate surface is proportional to the velocity gradient at the surface:

$$\tau_0 = -\mu \left(\frac{du}{dy} \right)_0$$

(2-81)

Due to skin friction, the fluid film acts as a dashpot dissipating the amount of energy, D:

$$D = \frac{1}{\omega} \int_0^{2\pi} \tau_0(\omega t) u(\omega t) d(\omega t)$$

(2-82)

The Q factor is related to the ratio of the strain energy stored in the system, W, to the energy dissipated through the plate area, A:

$$Q = \frac{2\pi W}{AD}$$

(2-83)

Couette-type model: The Couette model (Fig. 2.13a) results in a linear velocity profile for the fluid underneath the plate. The dissipated energy under plate is

$$D_{cd} = \frac{\pi}{\omega} u_0^2 \left(\frac{\mu}{d}\right)$$

(2-84)

For the ambient fluid above the plate, the velocity gradient is 0. The ambient fluid above the plate is considered to osculate in time with the plate motion, generating negligible amounts of viscous damping.

Stokes-type model: Stokes-type model (Fig. 2.13b) results in the velocity above the plate of:

$$du/dy = u_0 \sqrt{\omega/v} \phi(\omega,t)$$

(2-85)

Substituting this velocity profile into Eq. (2-81), we obtain the energy dissipated by the stokes-type damping in the ambient:

$$D_{y,\sigma} = \frac{\pi}{\omega} u_0^2 \mu \beta$$

(2-86)

where,

$$\beta = \sqrt{\omega/2v}$$

(2-87)

Its reciprocal indicates a distance over which the motion amplitude decreases by a factor of e.

Similarly, the energy dissipated underneath the plate is:

$$D_{sd} = \frac{\pi}{\omega}u_0^2\mu\beta\left(\frac{\sinh 2\beta d + \sin 2\beta d}{\cosh 2\beta d - \cos 2\beta d}\right)$$

(2-88)
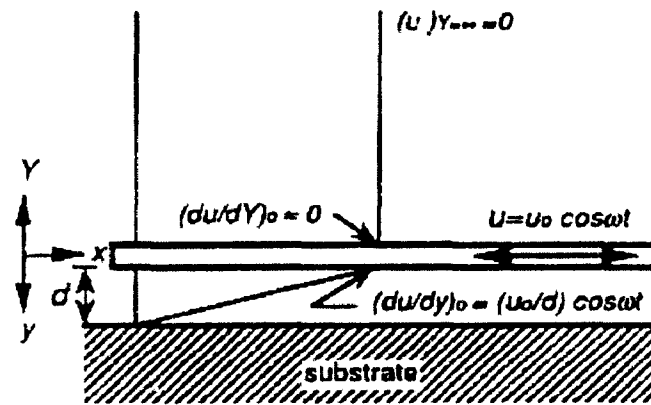
**(a) Couette-type**
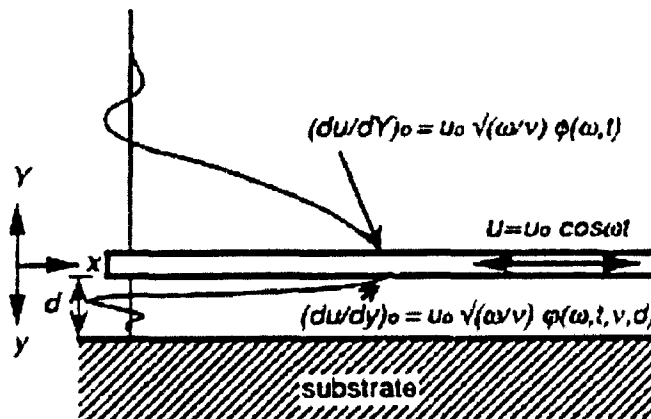
(b) Stokes-type

Figure 2.13 Sketch of Couette and Stokes models [24]

2.6.3 Q-estimation

Substitution of Eq. (2-83) into (2-82) results in the quality factor, Q_{cd}, due to the Qouette-type damper of thickness d:

$$Q_{cd} = \frac{d}{\mu A}\sqrt{MK}$$

(2-89)

For a Stokes-type damper, it is found that

$$\frac{Q_{s \cdot \infty}}{Q_{cd}} = \frac{1}{\beta d}$$

(2-90)

$$\frac{Q_{sd}}{Q_{cd}} = \frac{1}{\beta d} \left(\frac{\cosh 2\beta d - \cos 2\beta d}{\sinh 2\beta d + \sin 2\beta d} \right)$$

(2-91)

$Q_{s,\infty}, Q_{cd}$ are Stokes-type damping in the air layers above the plate and underneath the plate.

For a comb drive structure, we also need to consider the Stokes-type damping between the fingers, Q_{sc}

$$Q_{sc} = Q_{cd} \frac{A_{fingers}}{A} \frac{1}{\beta d} \left(\frac{\cosh 2\beta d - \cos 2\beta d}{\sinh 2\beta d + \sin 2\beta d} \right)$$

(2-92)

Then the overall Q factor resulted from a Stokes-type damper is estimated as:

$$\frac{1}{Q} = \frac{1}{Q_{sd}} + \frac{1}{Q_{s\infty}} + \frac{1}{Q_{sc}}$$

(2-93)

2.7 Structure design

Structure and geometries of the accelerometer could be designed as all the above physical principles are known.

This work is the initial stage of project, a tunneling accelerometer. The objective of the accelerometer is to achieve a resolution of acceleration of 1μg. The resolution is limited by the thermal mechanical noise. This noise could be expressed as an equivalent acceleration:

$$a = \sqrt{\frac{4 K_b T \sqrt{k}}{(m)^{3/2} Q}}$$

(2-94)

Where,

K_b is Bolzman constant.

T is temperature which is also a constant.

Q is the qualify-factor which is decided by the structure.

We cannot calculate or estimate it before the structure is decided. k is the spring constant and m is the mass of the proof-mass. k is decided by the geometry and material of the suspension beams.

Geometries of the beams are also constrained by the process possibilities. The main constraint is the aspect ratio. If the aspect ratio is too high it will bring difficulties to the processes such as sputtering, Inductive Coupled Plasma (ICP) etching, and hot embossing. The aspect ratio is limited less than 15. For the first trial, the minimum feature size is also limited at 5 μm. A commercial SOI wafer with thickness of top silicon of 60 μm (the reason that a SOI wafer is used will be addressed below in the process section). The thickness (or height) of the structure is decided by the SOI wafer at 60 μm. m is proportional to the volume and density of the material, PMMA, of the proof-mass. The area of m is mainly decided by the needed electrostatic force produced by the comb drive. The practice design is a trail and error process.

Spring constant k is set at 20 N/m based on the experiences first. Eq. (2-94) requires k as small as possible. However if k is too small the beams will be too "soft". Consequently, the beams (springs) might have no restoring force at all.

Our final objective of the accelerometer is to achieve a resolution of acceleration of 1 μg, which means that a is about 10^{-5} m/s^{-2}. According to the Eq. (2-94) we can get:

$$m \geq \left(\frac{16 k_h^2 T^2 K}{a^4 Q^2} \right)^{\frac{1}{3}} = \frac{3.8 \times 10^{-6}}{Q^{\frac{2}{3}}} \quad Kg$$

(2-95)

where,

$K_b = 1.38 \times 10^{-23}$,

$T = 300K$,

$K = 20N/m$

On the other hand, the range of accelerometer is set at 1 mg. The displacement of the proof-mass normally is limited within $1\mathring{A}$ because the exponential relationship between tunneling current and distance. Too large a moving distance will dramatically increase the nonlinearity.

$$\Delta y K_y = ma \qquad (2\text{-}96)$$

and

$$\Delta y \leq 1\mathring{A}$$,

Then

$$m \leq \frac{\Delta y K_y}{a} = \frac{1 \times 10^{-10} \times 20}{10^{-2}} = 2 \times 10^{-7} \quad Kg \qquad (2\text{-}97)$$

Now, from Eq. (2-93) and Eq. (2-95), Q should be larger than 83. Normally, this is a value that is easy to get.

For the next step, geometry of the beams, the number of the fingers of the comb drive and the driven voltage of comb drive should be decided. These values are estimated using analytical equations approximately first. Then ANSYS FEA software is used to decide them.

The spring constant of beams is governed by Eq. (2-54)

$$K = \frac{F}{y(l/2)} = \frac{32Ehw^3}{L^3}$$

Then,

$$L = \left(\frac{32Eh}{K}\right)^{\frac{1}{3}} \times w = \left(\frac{32 \times 2 \times 10^9 \times 60 \times 10^{-6}}{20}\right)^{\frac{1}{3}} \times w = 57.7w \tag{2-98}$$

Let $w = 15$ μm according to the experience, then L is about 860 μm.

The driven force of a comb drive is described by Eq. (2-57)

$$F_{Total} = -\frac{n\varepsilon h}{g}V^2$$

And,

$$F = Ky \cdot \Delta y = 20 \times 5 \times 10^{-6} = 1 \times 10^{-4} N$$

Then,

$$n = \frac{Fg}{V^2\varepsilon \cdot h} = \frac{1 \times 10^{-4} \times 10 \times 10^{-6}}{V^2 \times 8.854 \times 10^{-12} \times 60 \times 10^{-6}} = \frac{1.88 \times 10^6}{V^2} \tag{2-99}$$

Let $V = 100$, then a comb drive with 200 units of fingers is needed. In other word, a comb drive that has 400 fingers is necessary.

Knowing these rough figures, an accurate adjustment can be done using the ANSYS FEA software. During adjustment, the following constraints should be kept in mind:

1. The minimum feature size

2. The aspect ratio

3. The affect on the vibration modes from the structure layout

To adjust the spring constant, the following three parameters can be adjusted: beam length, beam width, and the width of the middle connection bar. After deciding the spring constant, the layout of the comb drive can be designed. Because half of the comb drive is also one part of the proof-mass, we need to adjust it carefully so that the mass of the proof-mass and the vibration modes are both satisfied. After many trials, we decided the structure layout as shown in Fig. 2.1.

In Fig.2.1, the total 150 units of fingers were decided for the consideration of the structure shape. Then the estimated actuation potential should be about 110 V.

For the next step we need to check if this structure satisfies other limitations.

First we need to check if the Strain and Stress exceed the breakdown limitations of the material PMMA. The strain and stress under the maximum loadings of 0.063% and 2.5MPa, respectively, was obtained in ANSYS simulation. They are much less than the stain and stress at break of 3.5% and 71MPa.

Then we need to check the stability of the comb drive as discussed in section 2.5.2.3. The spring constant in x direction is 2965N/m.

$$\frac{x^2 K_x}{g^2} = \frac{2695 \times (10 \times 10^{-6})^2}{(25 \times 10^{-6})^2} = 431.2 >> K_y = 20$$

For the comb drive we also have to make sure that the driving force in $+y$ direction is much larger than that in $-y$ direction. Otherwise the beams will not be deformed in the $+y$ direction as we wish. The driving force in $-y$ direction results from the neighbor comb drive units. They are the closing gap type comb drive.

$$F_{y^+} = \frac{N \varepsilon \varepsilon_0 V^2 h}{2d} = \frac{30 \times 8.854 \times 10^{-12} \times 110^2 \times 60 \times 10^{-6}}{2 \times 10 \times 10^{-6}} = 1.1 \times 10^{-5}$$

and

$$F_{y^-} = \frac{A \varepsilon \varepsilon_0 V^2}{s^2} = \frac{60 \times 10^{-6} \times 600 \times 8.854 \times 10^{-12} \times 110^2}{(65 \times 10^{-6})^2} = 1.1 \times 10^{-6}$$

Thus

$$F_{y^+} > 10 F_{y^-}$$

And it is satisfied.

In our design the fixed fingers of the comb drive are fixed at one end with a fixed bank. The fingers and the lateral beams on which they are attached are also suspended. In other words, they can also bend like a one-end-fixed beam under electrostatic force. The beams should be rigid enough to prevent from being bended too much. Otherwise, two set of fingers will contact with each other and result in a short of the circuit. The analytical equation of the bending for one end fixed beam is:

$$y_{max} = \frac{qL^4}{8EI} = \frac{12FL^3}{8Ehw^3}$$

(1-100)

Where, q is the uniform distributed loading. Applying in the figures in our design we get:

$$y_{max} = \frac{qL^4}{8EI} = \frac{12FL^3}{8Ehw^3} = \frac{12 \times 9.3 \times 10^{-6} \times (600 \times 10^{-6})^3}{8 \times 2.5 \times 10^9 \times 60 \times 10^{-6} \times (50 \times 10^{-6})^3} = 1.6 \times 10^{-7} = 0.16um$$

The ANSYS simulation result is: $y_{max} = 0.152$ μm. Thus, they are both small enough.

Another thing we need to check is the bending of the end fingers. As mentioned previously, the electrostatic force on the end fingers cannot be counteracted. It is very difficult to calculate the bending by analytical equations because it is a problem under coupled multiple physical fields. The electrostatic force will bend the beam first. Then the bended beam will result in the closer of the beans which will further bend the beam till they get an equilibrium position. Fortunately, ANSYS can do this problem easily. The simulation result is $y_{max} = 0.015$ μm, which is also small enough compared the gap distance of 10 μm.

A modal analysis is necessary to check if the first vibration mode is the desired mode. The ANSYS simulation results were positive (the detailed results are presented in the simulation section).

Finally, we still need to check the *Q*-factor based on the designed structure.

a) Squeeze-film damping

The squeeze-film damping requires that movement should be small compared to its dimension and that the Reynolds number should be smaller than 1. The movement is only in the Angstrom range in our design. The Reynolds number is defined by Eq. (2-74). In our design, the vibration frequency ω is 3000 x 2 x3.14, which results in the velocity of the air molecule of 10^{-9} x 3000 x 2 x3.14. The thickness of air layer d is 30 or 70 μm. The air viscosity is 1.8 x 10^{-5} Ns/m^2. Thus, the Reynolds number should be:

$$R_s = \frac{z_0 \rho \omega}{\mu} = \frac{70 \times 10^{-6} \times 3000 \times 6.28 \times 1.225}{1.8 \times 10^{-5}} = 9 \times 10^{-5} < 1$$

Now the squeeze-film damping can be estimated. For the squeeze films between the fingers tips and their corresponding side walls of the beams, we have:

$y = 600$ μm, $x = 60$ μm, and $d_0 = 30$ μm

Thus $y >> x$

Then for one arm, according to Eq. (2-78) we have:

$$D_s = 1 \times \left(\frac{\mu y x^3}{d_0^3} \right) = \frac{1.8 \times 10^{-5} \times 600 \times 10^{-6} \times (60 \times 10^{-6})^3}{(30 \times 10^{-6})^3} = 8.64 \times 10^{-8} Ns/m$$

There are 11 pairs of arms totally

$$D_s = 11 \times 8.64 \times 10^{-9} Ns/m = 9.5 \times 10^{-7} Ns/m$$

For the squeeze films between the arms we have:

$y = 600$ μm, $x = 60$ μm, and $d_0 = 70$ μm

Also $y >> x$

Then for one pair of arms:

$$D_s = 1 \times \left(\frac{\mu y x^3}{d_0^3} \right) = \frac{1.8 \times 10^{-5} \times 600 \times 10^{-6} \times (60 \times 10^{-6})^3}{(70 \times 10^{-6})^3} = 6.8 \times 10^{-9} \, Ns/m$$

There are 10 pairs of arms in total

$$D_s = 10 \times 6.8 \times 10^{-10} = 6.8 \times 10^{-8} \, Ns/m$$

Then the total damping factor from the squeeze film is:

$$D_{s-total} = 9.5 \times 10^{-7} + 6.8 \times 10^{-8} = 1.02 \times 10^{-6} \, Ns/m$$

And the total damping coefficient from the squeeze film is:

$$\zeta = \frac{D_{s-total}}{2\sqrt{MK}} = \frac{1.02 \times 10^{-6} \, Ns/m}{2\sqrt{6.55 \times 10^{-8} \, Kg \times 20 N/m}} = 4.46 \times 10^{-4}$$

Then the Q-factor would be:

$$Q_s = 1/2\zeta = 1/(8.92 \times 10^{-4}) = 1122$$

b) Laterally oscillating viscous damping

From the Eq. (2-80) we know:

$$v = \mu/\rho = \frac{1.8 \times 10^{-5} \, Ns/m}{1.225 Kg/m^3} = 1.47 \times 10^{-5} \, Nsm/Kg$$

According to Eq. (2-87)

$$\beta = \sqrt{\omega/2v} = \sqrt{3000 \times 6.28 s^{-1}/2 \times 1.47 \times 10^{-5} \, Nsm/Kg} = 25314 m^{-1}$$

Then,

$$\beta d = 25314 m^{-1} \times 50 \times 10^{-6} m = 1.266$$

From Eq. (2-89) to Eq. (2-92) we can get:

$$Q_{cd} = \frac{d}{\mu A}\sqrt{MK} = \frac{50 \times 10^{-6}}{1.8 \times 10^{-5} \times 9.25 \times 10^{-7}}\sqrt{6.55 \times 10^{-8} \, Kg \times 20 N/m} = 3437$$

$$Q_{s \cdot \infty} = Q_{cd} \frac{1}{\beta d} = \frac{3437}{1.266} = 2715$$

$$Q_{sd} = Q_{cd} \frac{1}{\beta d} \left(\frac{\cosh 2\beta d - \cos 2\beta d}{\sinh 2\beta d + \sin 2\beta d} \right) = \frac{3437}{1.266} \times 1.048 = 2845$$

$$Q_{sc} = Q_{cd} \frac{A_{fingers}}{A} \frac{1}{\beta d} \left(\frac{\cosh 2\beta d - \cos 2\beta d}{\sinh 2\beta d + \sin 2\beta d} \right) = \frac{864000}{924800} \times 2845 = 2658$$

Then from the Eq. (2-93) we can get the total Q-factor

$$\frac{1}{Q_L} = \frac{1}{2715} + \frac{1}{2845} + \frac{1}{2658}$$

And, $Q_L = 912$

The final total Q would be

$$Q_{Final} = Q_s \times Q_L / (Q_s + Q_L) = 503$$

Now we can go back to check if the Q and M satisfy Eq. (2-95) and Eq. (2-97).

Applying $Q = 503$ into Eq. (2-95) we get

$$m \geq \frac{3.8 \times 10^{-6}}{503^{\frac{2}{3}}} = 6.0 \times 10^{-8} Kg$$

The mass of our designed structure is $M = 6.55 \times 10^{-8} Kg$. $6.0 \times 10^{-8} \leq M \leq 2 \times 10^{-7}$, indicating that it is satisfied.

CHAPTER THREE

FINITE ELEMENT SIMULATIONS

3.1 Static Analysis

Finite Element Analysis (FEA) simulates loading conditions and determines a response to those conditions. In a FEA simulation, the engineering structures are modeled as a series of individual members, or, in other words, discrete building blocks called elements which are connected together at a number of points. Such structures are called *skeletal structures*. The points at which the individual members are joined are referred to as *node points*. Each element has exact equations that describe how it responds to a certain load. The "sum" of the response of all elements in the model gives the total response of the whole structure design. The elements have a finite number of unknowns, hence the name finite elements (Fig. 3.1).
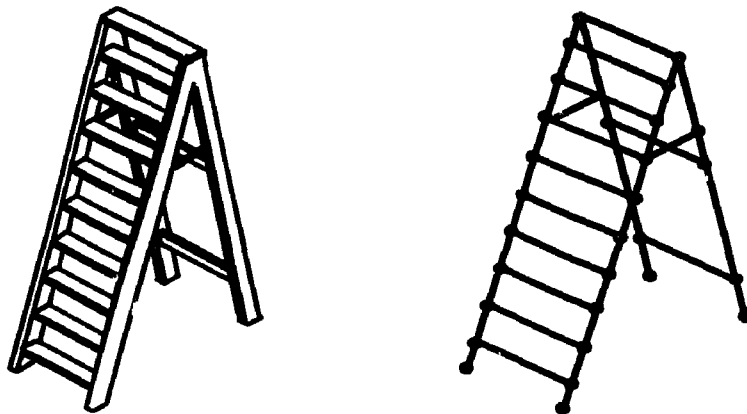

Figure 3.1   Physical system (left) and Finite element model (right)

When a structure is divided into many members, this type of approach can become very laborious and involve a large number of simultaneous equations for the solution. However, these problems can be solved very well by computers due to the large number of repetitive steps involved in the solution (matrix-method).

There are many advantages with the finite element simulation. It reduces the amount of prototype testing and allows multiple "what-if" scenarios to be tested quickly and effectively. It can also help us with the comparing of our engineering results with the theories so that we can understand our design and processes clearer.

In our project, we used ANSYS 5.7, which is a FEA software package that can simulate many fields of engineering.

A typical ANSYS analysis has three distinct steps: 1. Build the model. 2. Apply loads and obtain the solution. 3. Review the results. First the *"preprocessing"* is used to build the finite element model which includes the specification of the model geometry and the material properties, then the generation of the elements and nodes with *"meshing"*. The second phase is to apply the constraints and loads and then to get the solution. The last step is to review the results with *"post processing"*.

A static analysis calculates the effects of *steady* loading conditions on a structure, while ignoring inertia and damping effects, such as those caused by time-varying loads. A static analysis can, however, include *steady* inertia loads (such as gravity and rotational velocity), and time-varying loads that can be approximated as static equivalent loads (such as the static equivalent wind and seismic loads commonly defined in many building codes).

Static analysis is used to determine the displacements, stresses, strains, and forces in structures or components caused by loads that do not induce significant inertia and damping effects. *Steady* loading and response conditions are assumed; that is, the loads and the structure's response are assumed to vary slowly with respect to time. The kinds of loading that can be applied in a static analysis include: externally applied forces and pressures, Steady-state inertial forces (such as gravity or rotational velocity), Imposed (non-zero) displacements, Temperatures (for thermal strain), and Fluences (for nuclear swelling) [25].
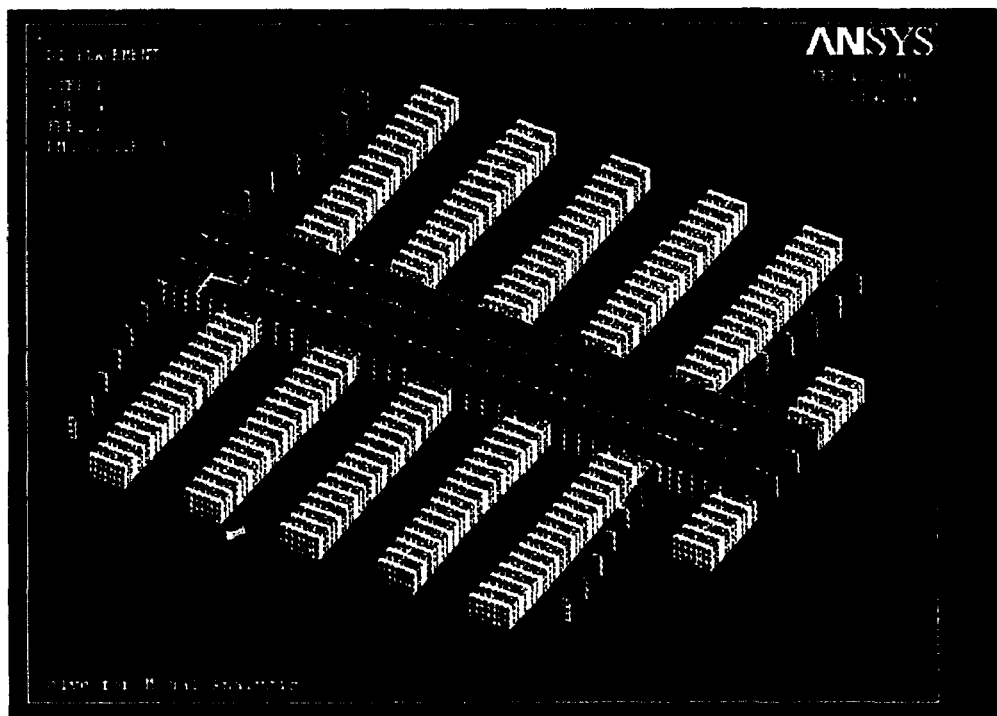

Figure 3.2   Mesh structure used in static analysis.

The *mesh* structure used in the static analysis in our work is shown in Fig. 4.2. Constrains were applied on the four ends of the beams. The force was applied on the end of the middle bar. The spring constant of the beams can be calculated from the applied force and the maximum displacement, which is

$$K = Force / Displacement$$

Actually, this simulation is used to optimize the structure and spring constant during the structure design period.

The static analysis is also used to verify whether the maximum stress and strain exceed the limitation of the tolerance of the material, PMMA. The results are shown in Figure 4.3

From the simulation results we can see that the maximum stress under maximum force is about 2.1MPa, which is much less than the stress at break, 71MPa, of the PMMA material. The maximum strain under maximum force is about 0.081%, which is much less than the strain at break, 3.5%.
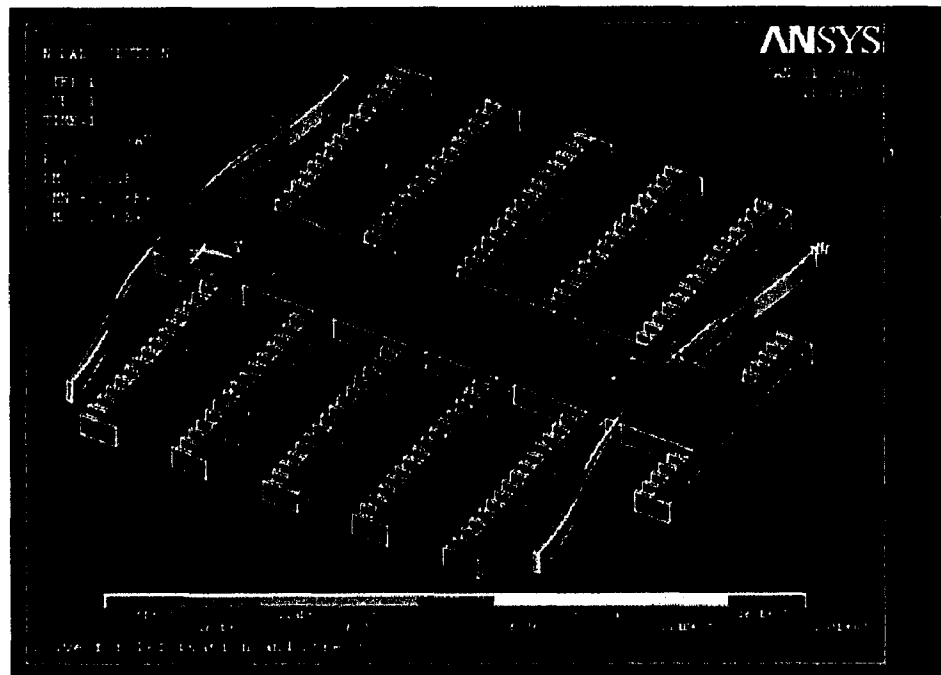
(a) Stress distribution under maximum force
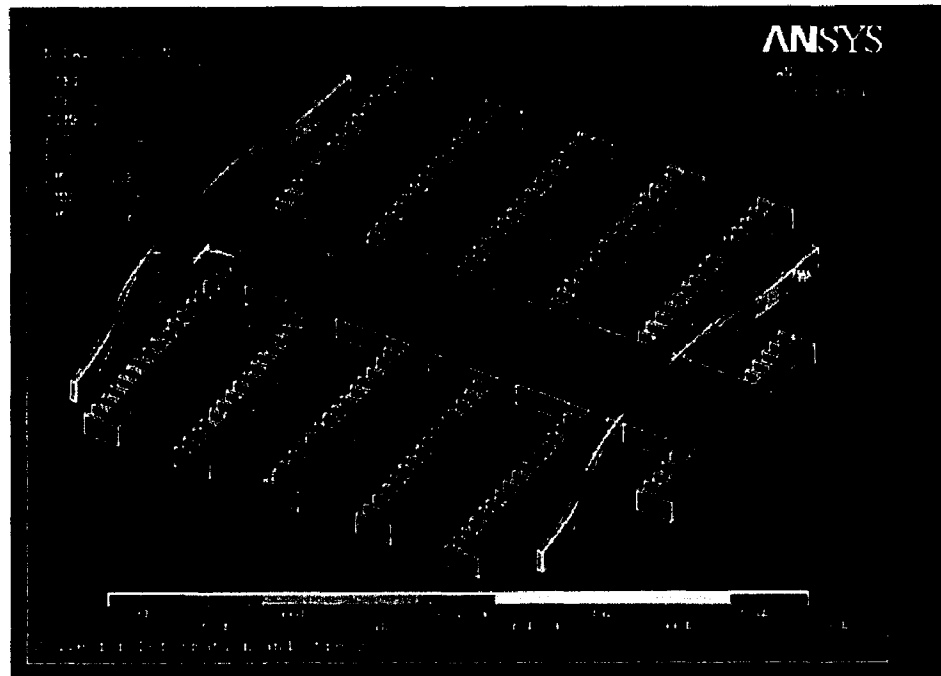
(b) Strain distribution under maximum force

Figure 3.3   Stress and strain distribution under maximum force

3.2 Modal Analysis

Modal analysis helps to determine the vibration characteristics (natural frequencies and mode shapes) of a structure or a machine component. It also can be a starting point for another, more detailed, dynamic analysis, such as a transient dynamic analysis, a harmonic response analysis, or a spectrum analysis.

The natural frequencies and mode shapes are important parameters in the design of a structure for dynamic loading conditions. They are also required before a spectrum analysis or a mode superposition harmonic or transient analysis is to be done.

The Modal analysis in the ANSYS family of products is a linear analysis. Any nonlinearities are ignored even if they are defined. The damped methods allow you to include damping in the structure. Modal analysis can also be performed on a pre-stressed structure.
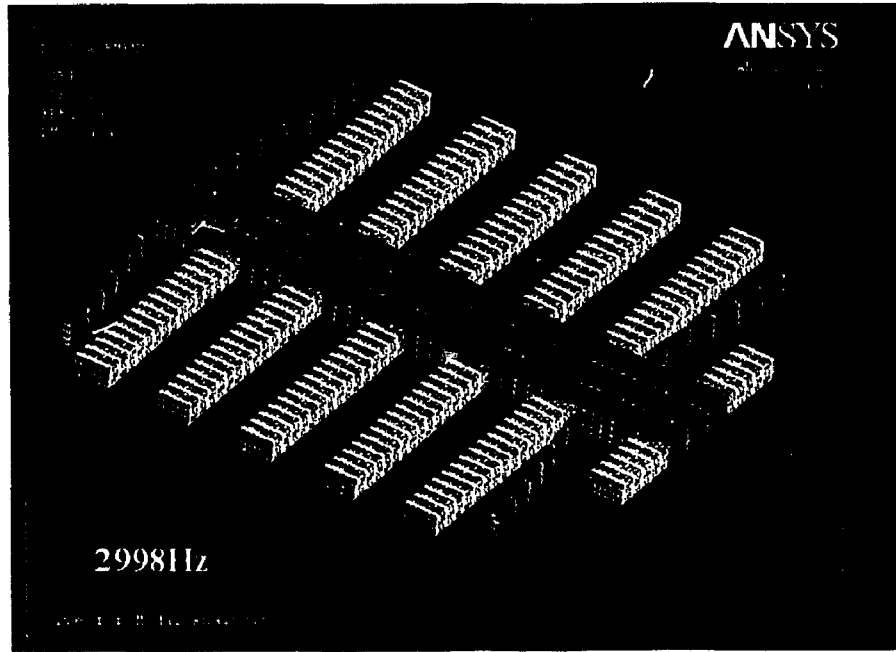
(a) 1st mode at resonance of 2998Hz
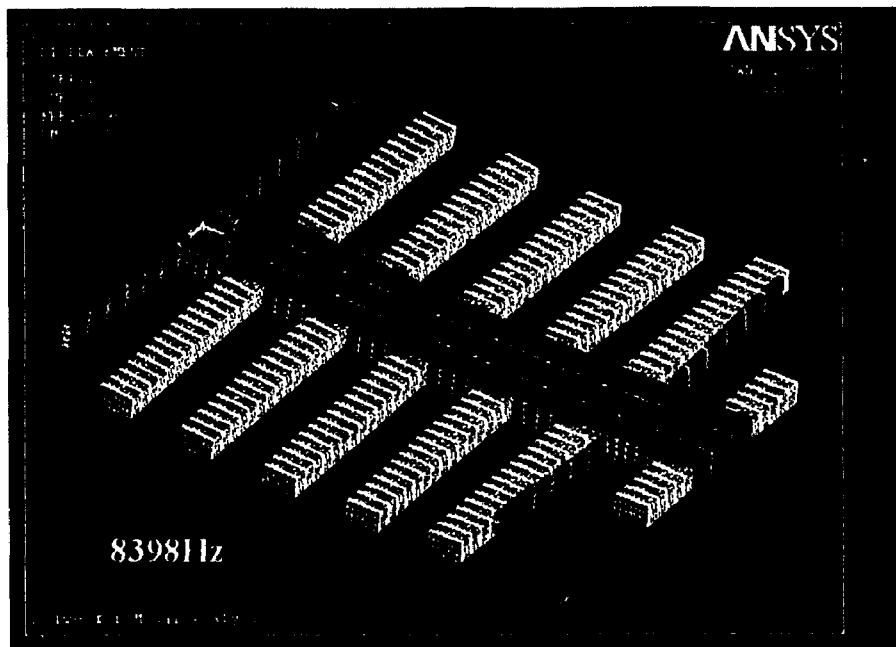
(b) 2nd mode at resonance of 9398Hz
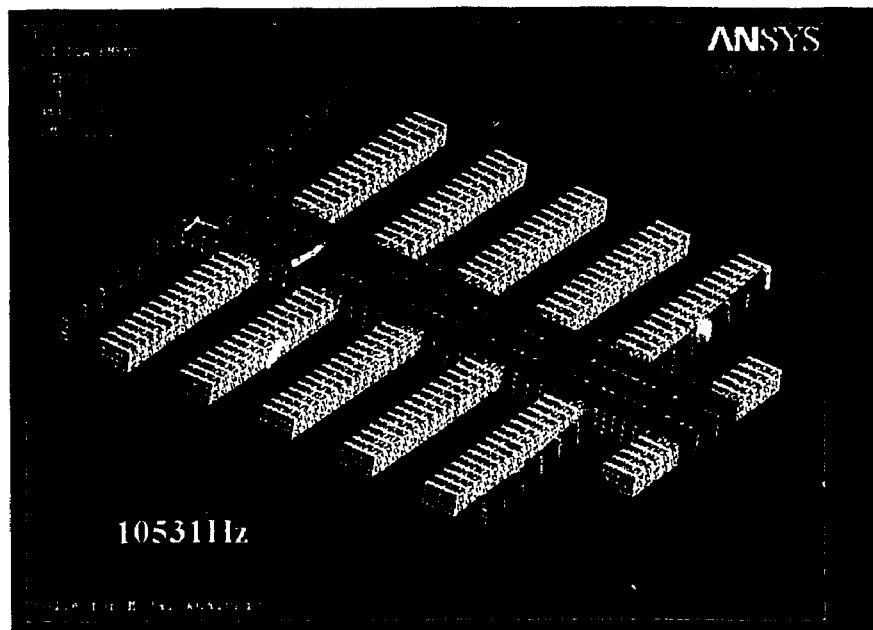
(c) 3rd mode at resonance of 10531Hz
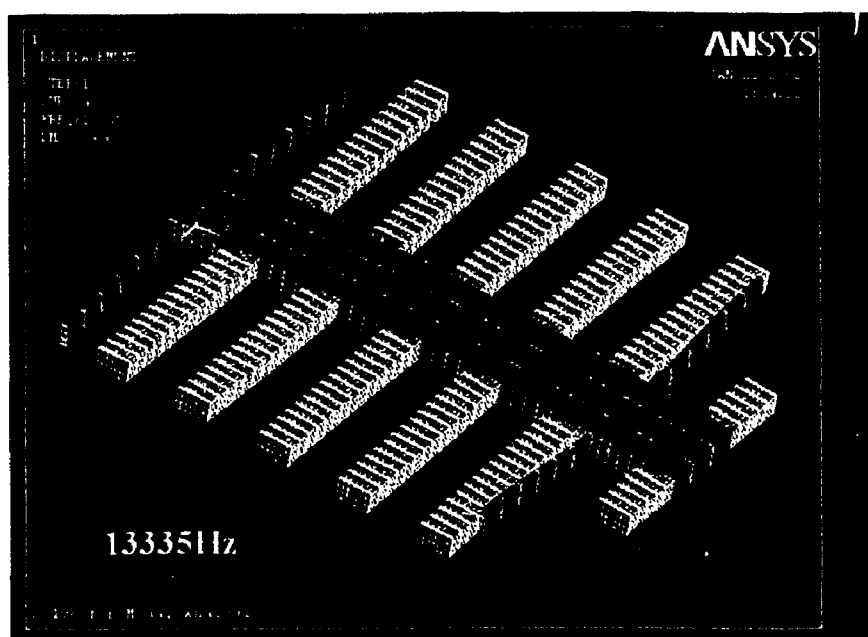
4th mode at resonance of 13335Hz

Figure 3.4 First 4 resonance frequencies and mode shapes

Fig. 3.4 shows the vibration resonance frequencies and the corresponding mode

shapes as a result of modal analysis carried out on a structure with the same element

mesh as it was specified in the static analysis. A damping ratio of 1×10^{-4} was used, which was obtained from the calculation in section 2.7.

From the results we can see that the first mode is our desire vibration mode. And the second resonant frequency is far away from the first resonant frequency, $F_2 > 3F_1$.

3.3 Harmonic response analysis

Harmonic response analysis gives us the ability to predict the sustained dynamic behavior of structures, thus enabling us to verify whether or not our designs will successfully overcome resonance, fatigue, and other harmful effects of forced vibrations.

Harmonic response analysis is a technique used to determine the steady-state response of a linear structure to loads that vary sinusoidally (*harmonically*) with time. The idea is to calculate the structure's response at several frequencies and obtain a graph of some response quantity (usually displacements) versus frequency. "Peak" responses are then identified on the graph and stresses reviewed at those peak frequencies.

This analysis technique calculates only the steady-state, forced vibrations of a structure. The transient vibrations, which occur at the beginning of the excitation, are not accounted for in a harmonic response analysis.

Harmonic response analysis is a linear analysis. Any nonlinearitis will be ignored, even if they are defined. Harmonic analysis can also be performed on a pre-stressed structure.

In many cases, harmonic response analysis is used to overcome problems such as breaking or fatigue of a structure but it can also be used to predict the sensitivity of the sensor.

Table 3.1 Simulation results for amplitude at different frequency

Frequency (Hz)	Amplitude (m)	Frequency (Hz)	Amplitude (m)	Frequency (Hz)	Amplitude (m)
100	9.88E-11	2100	1.88E-10	4100	1.21E-10
200	9.91E-11	2200	2.07E-10	4200	1.09E-10
300	9.97E-11	2300	2.30E-10	4300	9.91E-11
400	1.00E-10	2400	2.61E-10	4400	9.05E-11
500	1.01E-10	2500	3.03E-10	4500	8.32E-11
600	1.03E-10	2600	3.65E-10	4600	7.68E-11
700	1.04E-10	2700	4.63E-10	4700	7.13E-11
800	1.06E-10	2800	6.42E-10	4800	6.63E-11
900	1.08E-10	2900	1.07E-09	4900	6.20E-11
1000	1.11E-10	3000	3.46E-09	5000	5.81E-11
1100	1.14E-10	3100	2.63E-09	5100	5.46E-11
1200	1.17E-10	3200	9.35E-10	5200	5.14E-11
1300	1.21E-10	3300	5.62E-10	5300	4.85E-11
1400	1.25E-10	3400	3.98E-10	5400	4.59E-11
1500	1.30E-10	3500	3.06E-10	5500	4.36E-11
1600	1.36E-10	3600	2.47E-10	5600	4.14E-11
1700	1.43E-10	3700	2.06E-10	5700	3.93E-11
1800	1.52E-10	3800	1.77E-10	5800	3.75E-11
1900	1.62E-10	3900	1.54E-10	5900	3.58E-11
2000	1.74E-10	4000	1.36E-10	6000	3.42E-11

The damping coefficient cannot be obtained from ANSYS 5.7 directly. The analytical calculated damping coefficient with value of 1×10^{-4} was input in the harmonic response simulation. The results are listed in table 3.1.

Fig. 3.5 shows the curve for the harmonic amplitude response with the frequency form 0 to 4 KHz. We can see from the table or chart that the resonant peak is close to 3 KHz. which agrees with prior Modal analysis. The amplitude response has a fair linearity below the frequency of 1 KHz.
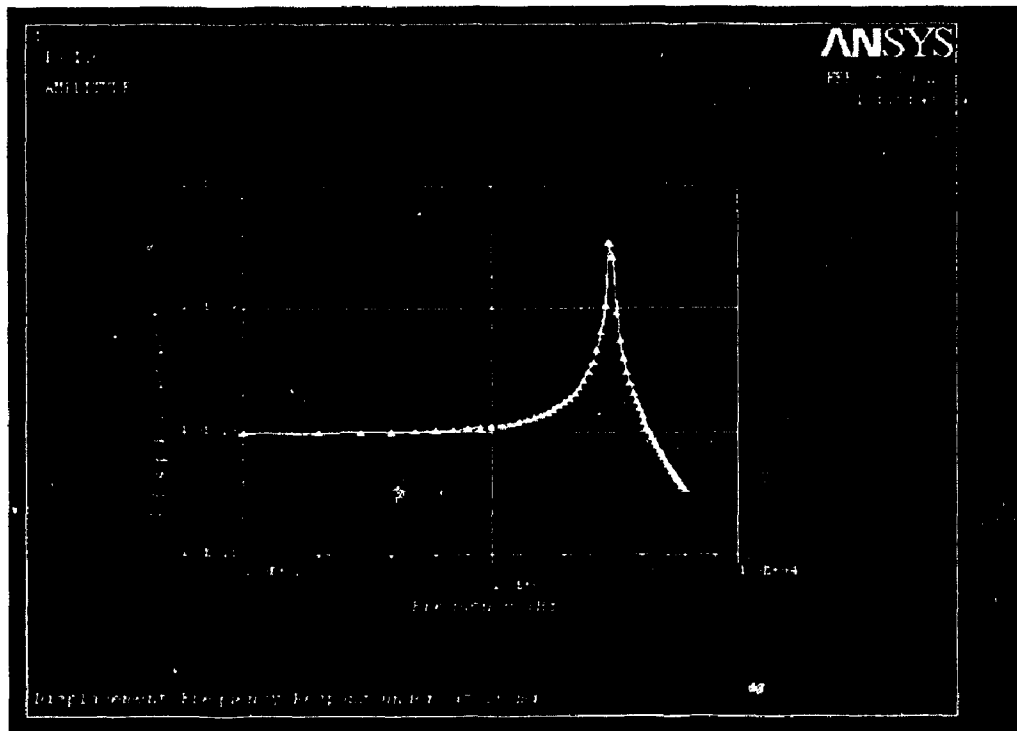
Figure 3.5   Harmonic amplitude response

3.4 Comb drive force analysis

Comb drive simulation in ANSYS is included in the electrostatic filed analysis domain. Electrostatic field analysis determines the electric field and electric scalar potential (voltage) distribution caused by charge distributions or applied potential. Two electrostatic analyses methods are available in ANSYS: The traditional h-Method and p-Method.

The p-method obtains results such as potential (voltage), electric field, electric flux density, electrostatic force or energy to your required degree of accuracy. To calculate these results, the p-method employs higher order polynomial levels (p-levels) of the finite element shape functions to approximate the real solution.

This feature works by taking a finite element mesh, solving it at a given p-level, increasing the p-level selectively, and then solving the mesh again. After each iteration,

the results are compared for convergence against a set of convergence criteria. The convergence criteria can be specified to include potential, electric field, or electric flux density at a point (or points) in the model, global-stored energy and global forces on a body (Maxwell Stress Tensor). The higher the p-level is used, the better the finite element analysis approximates to the real solution.

The p-method solution option offers many benefits for electrostatic analyses that are not available with the traditional h-method. The most convenient benefit is the ability to obtain good results to a desired level of accuracy without rigorous user-defined meshing controls.

In addition, the p-method adaptive refinement procedure offers error estimates that are more precise than those of the h-method, and can be calculated locally as well as globally (for example, total force on a body rather than electrostatic energy). For example, if one needs to obtain highly accurate solutions at a point, such as for dielectric breakdown, or forces on a body, the p-method offers an excellent means of obtaining these results to the required accuracy [26]. Thus in our simulation the p-method is used.

As mentioned in section 2.5.2.2, for a laterally driven comb drive we should know the constant force region. A 3-dimensional model is used to estimate the constant force region because there are only two 3-D elements for the p-method simulation in ANSYS. There is no 2-D element fc he p-method. The model is shown in Fig. 3.6. The structure parameters are as follows:

Finger length:	$L=20\ \mu m$
Finger width and gap:	$d=g=1\ \mu m$
Finger height.	$h=1\ \mu m$
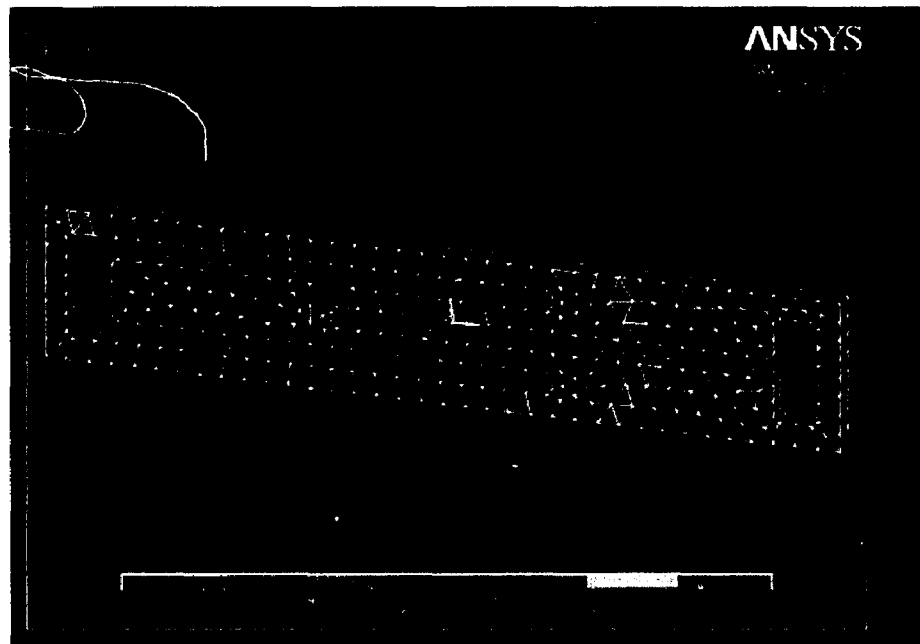
Figure 3.6   Mesh and elements with their p-levels

In the model, the corners are trimmed with radii of ¼ width of the fingers. One reason for trimming the corners is that it is required by the simulation. In ANSYS, in order to get the driving force, it is necessary to apply Maxwell Force Flags on the surface of the desired components, in our case, the moving fingers. The flags indicate the surface on which the electrostatic force distribution is to be calculated. Then elements with flagged surfaces will have surface forces computed and stored. ANSYS calculates forces by the Maxwell stress tensor approach and stores them in the air elements. The total force applied on the desired components is achieved by summing the forces on each node of the flagged elements. These forces can be applied to the structure components automatically as loads in a structural analysis sequence during the coupled-filed analysis. If the corners are squares, the Maxwell stress tensor method is unable to accurately capture the concentrated force at the corner of the finger. This will result in a simulation value of the driving force of about 30% less than the theoretical value. By trimming the

corners, the simulation values differing from theoretical ones within 2% can be obtained

easily by using the p-method with simple element mesh controls.

Another reason it is required to trim the corners is for the process of hot embossing.

Polymers are easily shrunk and can stick on the sharp corners of the mold. This will

result in the failure of the de-molding procedure.
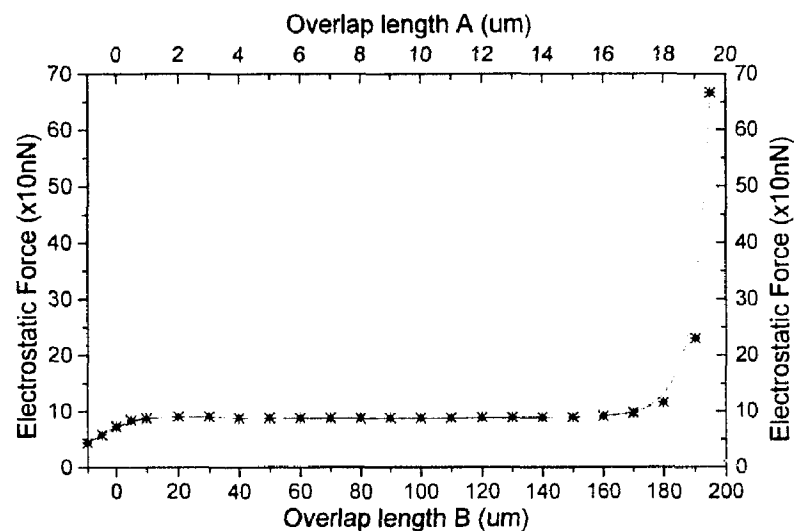
Figure 3.7 Drive force versus the overlap length.

Fig. 3.7 gives out two sets of results from different structures with the same

dimensional ratio. In structure A the dimensions are: $L=$ 1 μm, $d=g=1$ μm, $h=1$ μm; In

structure B the dimensions are: $L=200$ μm, $d=g=10$ μm, h=10 μm. The applied voltages

are 10 V in both cases. The results indicate know that for a comb drive with the same gap

distance and finger width of g, it enters the linear region from overlap length $2g$. And the

linear region stops at $3g$ before the finger ends closing to the inside surfaces of the

support beams.

Fig. 3.8 shows the potential distribution along the x-direction.
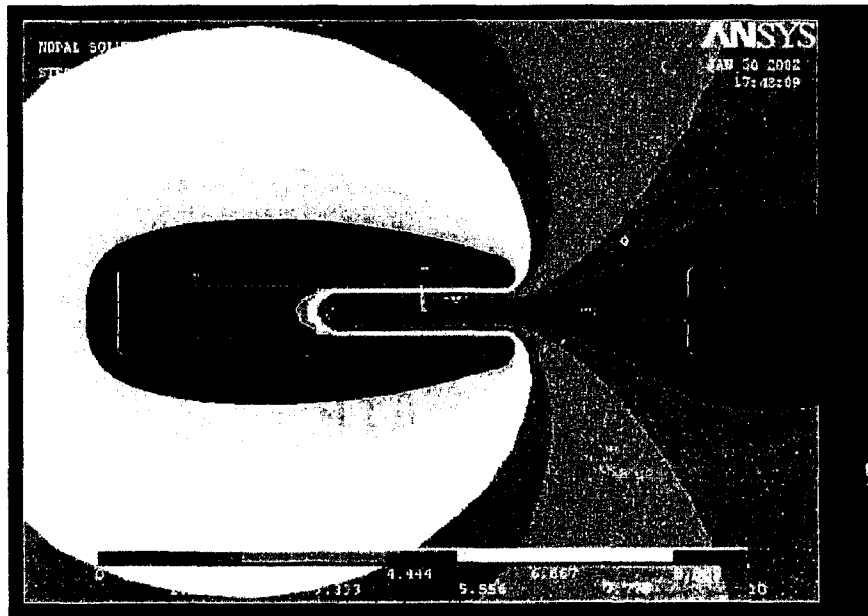
Figure 3.8 Potential distribution of a unit comb drive

Another issue in comb drive design that one should address is the problem of pull-in as mentioned in section 2.5.2.1. This pull-in problem needs to be considered more carefully for polymer materials. Because it is much "softer" than silicon, a comb drive on a polymer is more easily affected by the pull-in problem.

The analysis of a pull-in problem belongs to the *coupled-field analysis* domain in ANSYS because it is a coupled multiple physical field. A *coupled-field analysis* is an analysis that takes into account the interaction (coupling) between two or more disciplines (fields) of engineering. In our case, it is the interaction between mechanical structure and electric field.

In ANSYS, coupled-field analysis includes two kinds of methods: *sequential coupled-field analysis* and *direct coupled-field analysis*. The sequentially coupled-field analysis refers to solving one physics simulation after another. Results from one analysis become loads for the next analysis. If the analyses are fully coupled, results of the

second analysis will change some input to the first analysis. The direct method for a coupled-field analysis involves a single analysis that uses a *coupled-field element*. There is no suitable coupled-field element for our case; thus, the sequential coupled method is used.

A two-dimensional model is enough for our case because the bending moment and electrostatic force in the *h* direction is linear. The model is shown in Fig. 3.9, which was further reduced to half structure because it can be taken as a symmetrical structure about *x* axial. The medium surrounding the fingers is meshed as air, which has a relative permittivity of 1. The bending finger is meshed as a polymer beam, which has Young's modulus of 3 x10^9 Pa and Poissison's ratio of 0.34. The moving finger is not meshed because it is an equi-potential body. The big circular region is reference ground area. The overlaid picture shows the local mesh. The voltage is applied to the outer surfaces of the two fingers. The results are shown in Fig. 3.10.
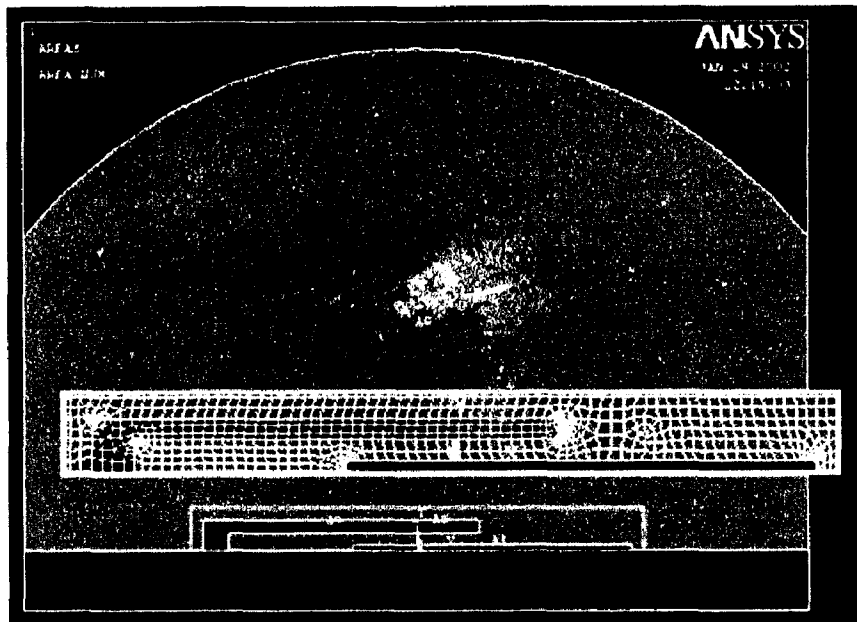

Figure 3.9 Model for pull-in problem in coupled-field analysis.
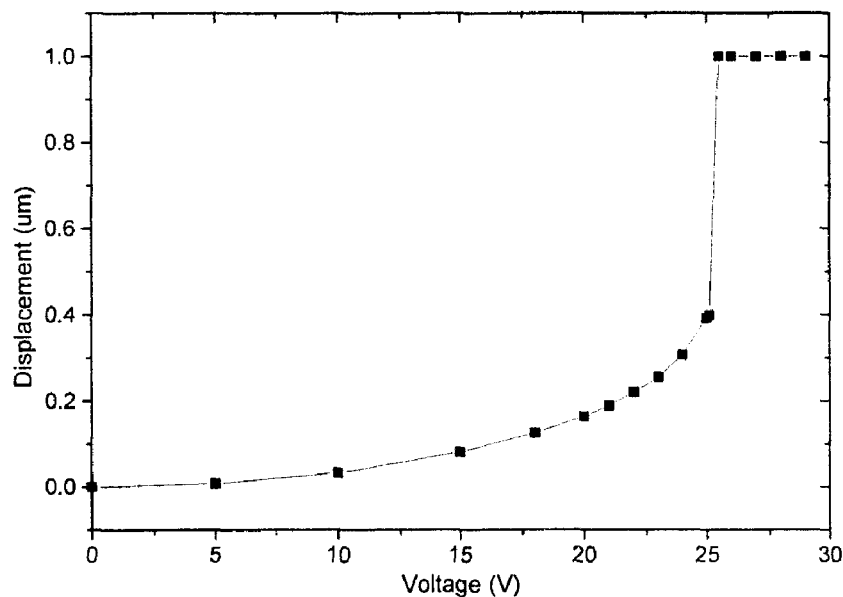
Figure 3.10 The relationship between bias voltage and bending.

We can see from Fig. 3.10 that for the given structure, finger length of 20 μm, both gap and finger thickness of 1 μm and overlap length of 10 μm, pull-in will occur when the bias voltage is around 25 V. For the comb drive with laterally driven, 25 V is a normal bias. So when a comb drive is designed on a polymer, the pull-in problem needs to be considered very carefully. For the same microstructure based on silicon, which has a Young's modulus around 170×10^9 Pa, the pull-in voltage is around 190 V. From another point of view, a polymer is more suitable worked as a micro-valve or a micro-switch because the pull-in voltage is much lower.

CHAPTER FOUR

DEVICE FABRICATION

4.1 Mold fabrication

Fabrication of a mold insert is necessary first in the hot embossing process. The basic

requirements for a mold insert are:

- Low mechanical stiction and friction.

- No deviation from vertical sidewalls (no undercuts)

- Smooth surfaces

- Defect free sidewalls

- Homogeneous material properties

- Chemically inert, avoid surface oxidation

4.1.1 Two kinds of mold inserts

There are mainly two kinds of methods to fabricate the microstructure mold for hot

embossing, metal molds, and silicon wafer molds.

For metal molds and rather large structures with dimensions of the order of 100um

and above, the conventional CNC-machining (Computer Numerical Control) methods in

materials such as stainless steel can be used. For smaller features, lithographical

techniques need to be employed. In lithographical techniques, the pattern is transferred

to a photoresist layer. A metal structure can be formed on the photoresist layer by electroplating. A metal mold is formed after resist removal.

Traditionally, for structures with a very high aspect ratio, the LIGA process is used to form a nickel mold. LIGA process uses high-energy X-ray radiation to expose a thick layer photoresist. A three dimensional resist structure with a very high aspect ratio (the thickness of the resist from microns to centimeters) could be formed after the exposure resist is developed. Subsequent electro-deposition fills the resist cavities with a metal, normally nickel or nickel oxide. After resist removal, a free standing metal stricture mold results. A typical LIGA process is illustrated in Fig. 4.1.
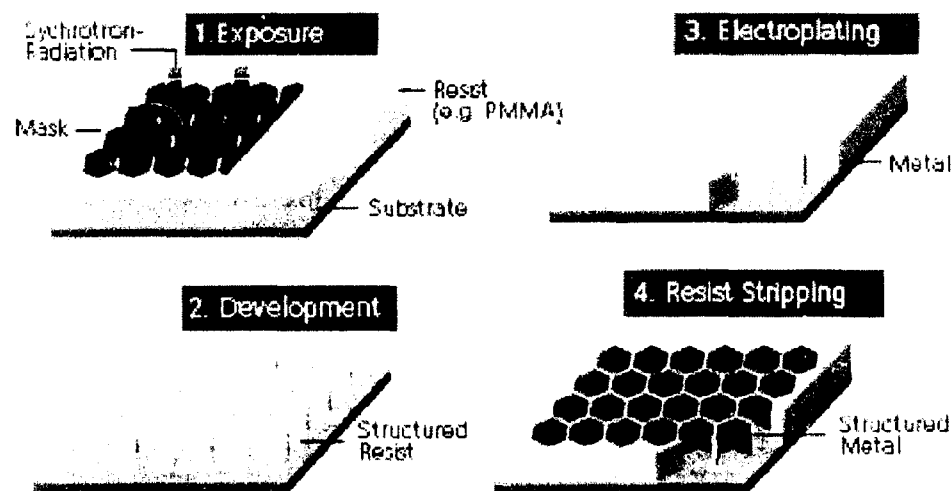

Figure 4.1 LIGA process[10]

Alternatively, the resist structure can be transferred onto silicon by means of dry or wet etching. This silicon structure now can be used directly as an embossing mold.

Normally, for mold insert fabrication on silicon wafer, the wet etching methods are limited because they are crystal orientation dependent etching (Fig. 4.2). Particularly, it is difficult to form vertical trenches with 90° side walls. Dry etching methods are desired

processes for formation of the silicon molds for they are crystal independent and vertical

trenches with high aspect ratio (up to >40:1) can be achieved.
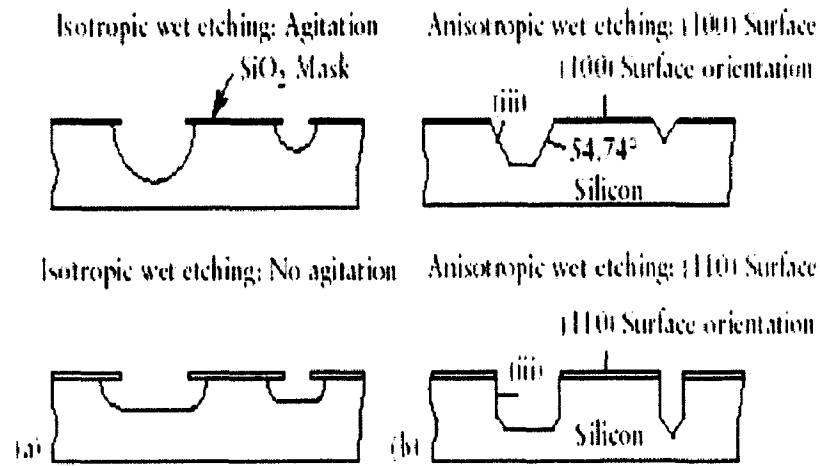
Figure 4.2 Crystal orientation dependent wet etching of silicon[27]

Nickel molds made by electroplating have several disadvantages[28]:

- Nickel is a relatively soft material, therefore prone to abrasion and wear. This will limit the number of replication cycles for a single mold.

- The electroplating process is slow. Therefore, the mold manufacturing is not well suited for rapid production, particularly in the case of structures with a high aspect ratio or large absolute heights (30 μm and above)

- In the electroplating process, voids within the mold can form in special geometries, particularly in high aspect ratio structures due to a nickel growth not only from the floor of the structure but also from the walls or due to different growth rates in the middle and close the wall of deep trenches.

- If the electroplating process happens on a silicon substrate, due to the growth mechanism of the nickel, high stresses are induced, which bend the substrate dramatically.

- The lithography process for the LIGA technique is extremely complicated and expensive.

For silicon mold insert fabricating, only lithography and etching are needed. Silicon molds have the following advantages:

- Suitable material mechanical and thermal properties in terms of hardness, tensile strength, linear thermal expansion coefficient, and thermal conductivity.

- Rapid and low cost fabrication due to the mature silicon processes. Variety of fabrication methods for different geometries readily available.

- Very flat and even surface, allowing for a good mold demolding.

Based on the above reasons, a silicon wafer mold is selected. The typical dry etching of Induct Coupled Plasma (ICP) process is used to fabricate our silicon mold. One can get very high aspect ration trench with 90° side wall profile with ICP. However, normally there are also some drawbacks for the ICP process.

4.1.2 Drawbacks of ICP process

Area dependent etching: Area dependent etching means that the etching depth is different for different open areas on the silicon wafer in the same process. In other words, the etching rate is faster for the wider trench than for the narrower trench (Fig. 4.3). The main reason is that the exchange rate for the reactive ion for etching Si on the wider trench bottom is faster than that on the narrower trench bottom [29].
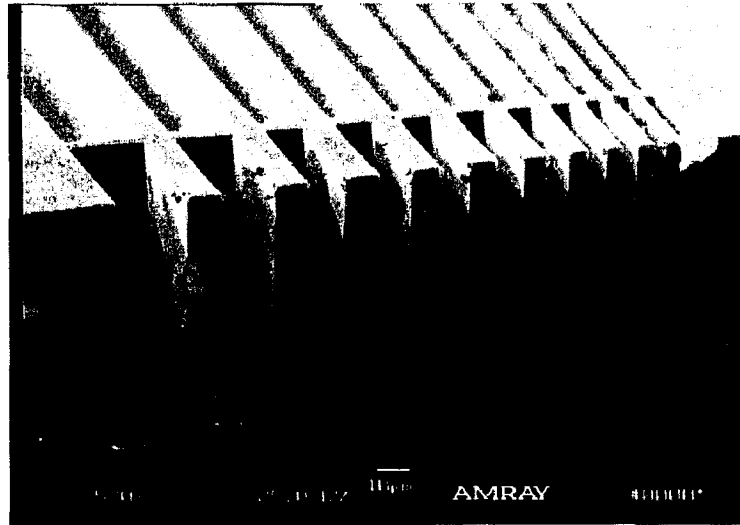
Figure 4.3 Area dependent etching

Another area dependent etching phenomena is that the profiles of the side wall are different between the narrow trench and wider open area. In our practice, the side walls in the big open area normally get undercut while the narrow trenches get vertical profiles (Fig. 4.4). The main reason for the undercut in the big open area is that the silicon wafer is often negative charged by the electrons. The incoming positive ions will be deflected towards the sidewall by the static electrical force. In the narrower trench, the negative potentials on the two closed sidewalls will be counteracted [29].
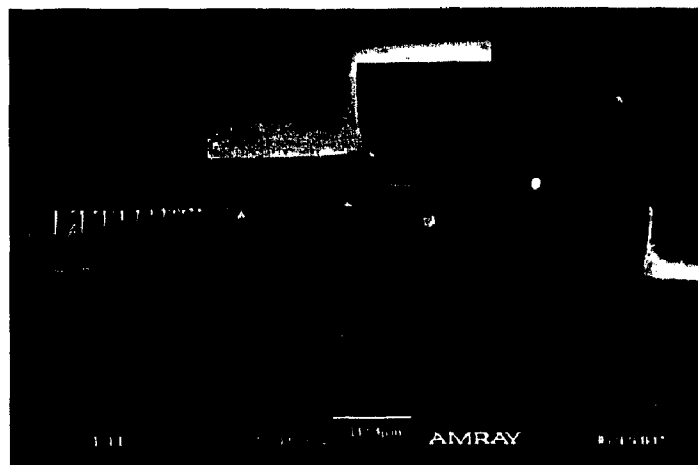

Figure 4.4 Undercut in the big open area

The first area dependent etching phenomena will result in the uneven height on the final polymer microstructures, the larger in area size, the larger in thickness (Fig. 4.5). This will further result in the difficulties either in design phase or in the backside process. The undercut in the big open area will cause problems in demolding process.

Micrograss: Micrograss often occurs in the bottom of the etched big open area. In an ICP process, there is the C_xF_y polymer deposition phase as well as the etching phase. Micro-masks could be formed in the deposition phase. In addition, micromasks could be also formed by masking material re-deposition [30]. The energetic reactive ions are highly collimated in ICP etching process. The energetic ions cannot strike on the silicon surface underneath the micro-masks, leaving them un-etched. Finally this un-etched silicon will become the micrograss (Fig. 4.6).
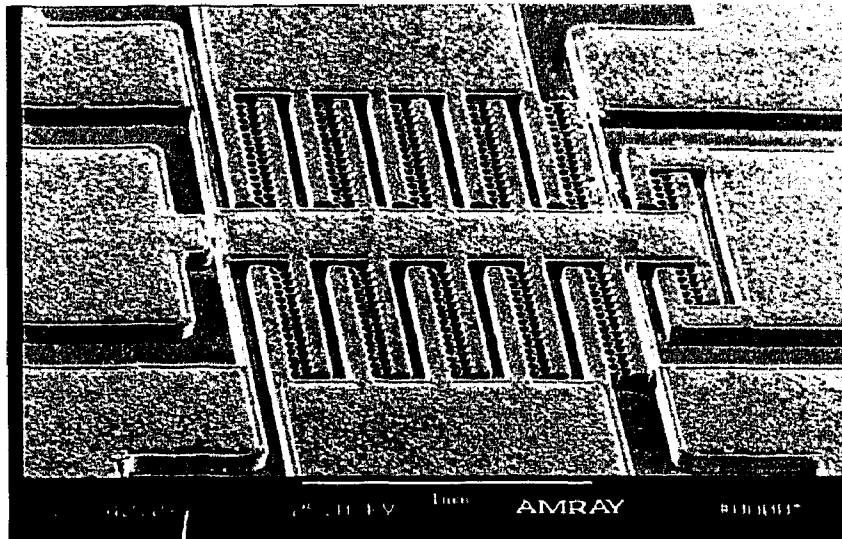

Figure 4.5   Uneven thickness in final PMMA structure

This micrograss not only could result in the coarse surface on embossed polymer structures but also could result in the failure of the demolding process.
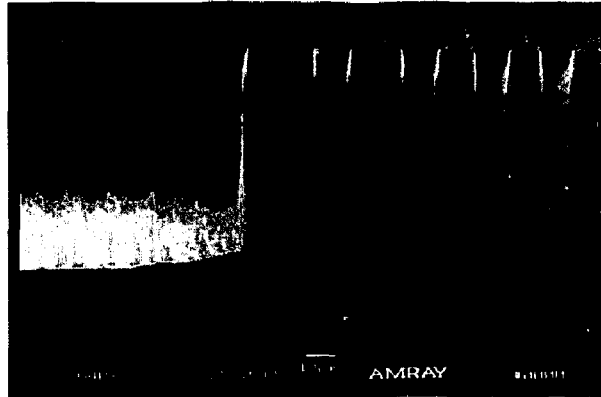
Figure 4.6   Micrograss in the bottom of big open area.

4.1.3 SOI wafer as mold insert

In order to overcome these problems resulting from the ICP process, we tried SOI wafers as the mold.   Our SOI wafer has the structure of $Si/SiO_2/Si = 60/2/400$ μm.   the etching will essentially stop at SiO_2 surface because the etching rate ratio of Si and SiO_2 is more than 100:1.   Thus, the final etching depth will be the thickness of the top Si layer no matter how big the opening pattern sizes are.   The smooth bottom surface could be also obtained by a certain mount of over etching.
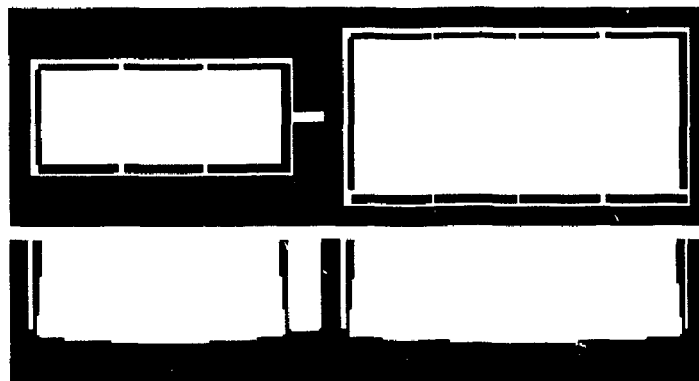

Figure 4.7   Assistant walls for compensating the undercut in big areas.

However, a SOI wafer still cannot eliminate the undercut in the big open areas.   This problem is solved by the mask design.   An assistant thin wall is added close to the side wall of the big area.   The distance between the thin wall and the side wall of the big open

area is several tens of microna so that a vertical trench could be obtained. The width of this assistant thin wall is decided by the total undercut. The best situation is to let assistant walls be etched through at the bottom in the end of the etching process. Even if there are several microns left at the bottom, these assistant walls will be easily removed by hot embossing during the first run because of the undercut. In our practice, the width of the assistant wall was 4 μm. This method is illustrated in Fig. 4.7.

4.1.4 Process of SOI wafer mold fabrication

First, a set of masks (two pieces) is designed and commercially fabricated. One mask is for the micro comb drive structure. One mask is for the substrate.

Positive resist 1813 with thickness of 2 to 3 microns was used in the lithography process. Then the wafer is put into ICP chamber. The high aspect ratio deep trench is achieved by the Bosch process. In the Bosch process, a fluorinated etching gas (SF_6) is used to etch silicon with a high etching rate yet isotropic. Several seconds later, SF_6 is cut off and C_4F_8, which is kind of polymer deposition gases, is fed in. A thin polymer passivation layer is deposited on the wafer, including the bottom and sidewalls of the previously etched trench. Then the SF_6 is fed in again. The fluorine radicals are able to break through the passivation on the bottom more readily because they are energetic ion-assisted. The passivation on the sidewalls remains intact because they are not bombarded directly by collimated energetic ions. Hence, the passivation is removed from the bottom of the trench first, and the fluorine attacks the silicon down further there. This continued switching between passivation and etching steps permits anisotropy (~90°) with high-rates.

The ICP system is Alcatel A-601 from Alcatel Vacuum Technology, France. The

SF_6/C_4F_8 gas system is used. The parameters of ICP process that we used were:

SF_6 : 300sccm/9seconds

C_4F_8 : 180sccm/4seconds

Throttle valve is opened at 35% all the time. The pressure is about 25mTorr

Source power 1800W

Bias power 30W resulting in the bias voltage around 50V

The temperature was controlled by the back side Helium gas whose temperature

was kept at 20°C by controlling the flow rate of liquid nitrogen and the power of the

heater.

The etching rate is about 4 μm/min. Process time is about 17 minutes. SOI wafer is

over etched for about 2 minutes to remove the micrograss on the bottom.

The schematics of these two processes are illustrated in Fig. 4.8. Fig. 4.8a shows the

final lithography process and 4.8b shows the final etching process.
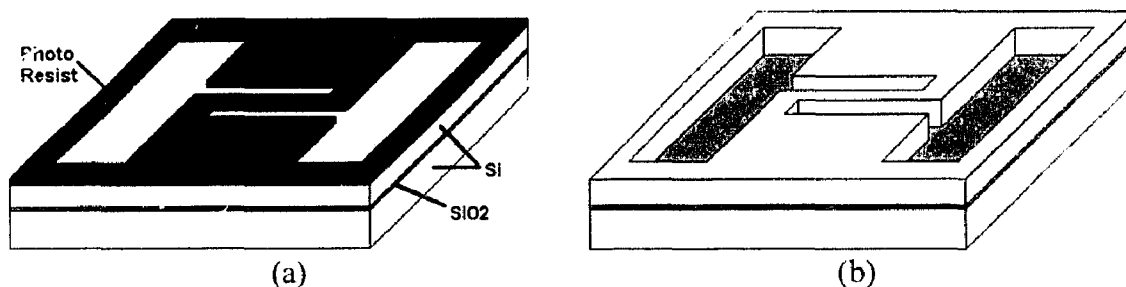

Figure 4.8   Sketch of Lithography and etching processes

Two SEM photos of a good result are shown in Fig. 4.9. From Fig. 4.9b we can see

some dark lines on the bottom closing to the side walls in big open areas. These lines

indicate the positions of the thin assistant walls, which were already etched off.
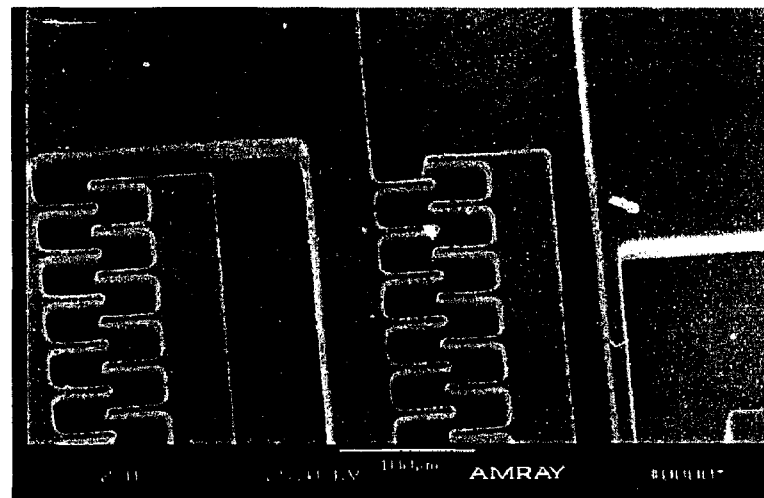
(a)
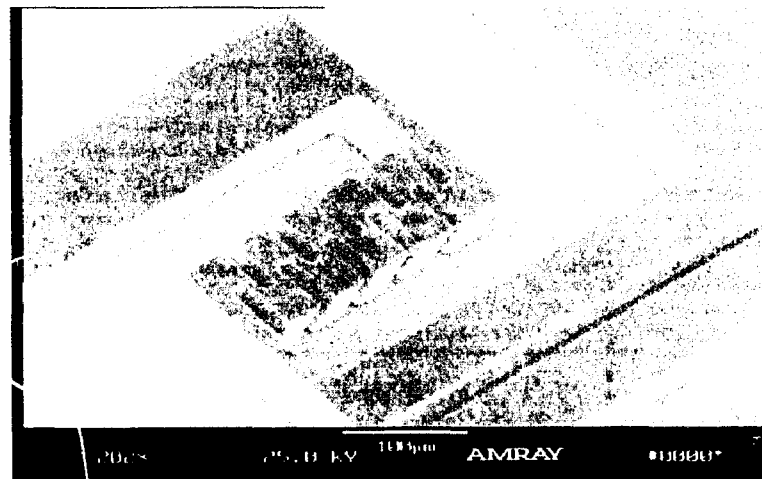
(b)

Figure 4.9   Evenness and smooth ICP etching on SOI wafer

4.2 Mold insert bonding

A SOI wafer itself is too thin and too fragile to be used as a mold insert. It is necessary to bond the silicon mold onto a thicker and stronger substrate to form a rigid mold insert. There are mainly two methods to do it. One is to bond the silicon wafer onto a Pyrex 7740 glass using anodic bonding technology. The advantage of this method for hot embossing process is that silicon and glass have a close thermal expansion coefficient. They can both endure high temperatures. The disadvantage is that the glass

is easily broken under high pressure. Because of this disadvantage and also because there is no anodic bonding system in our lab, we developed a new method, gluing silicon wafer onto a stainless steel disk.

The silicon wafer was glued onto a 5 mm thick stainless steel disk using high temperature glue (up to 300 °C) which was coated to both silicon and steel disk surfaces first. Then they were put on a hot plate. A small steel brick was put on top of the assembly to make two surfaces contacting tightly. Then the glue was cured under 120 °C for one hour. A completed mold insert is shown in Fig. 4.10.
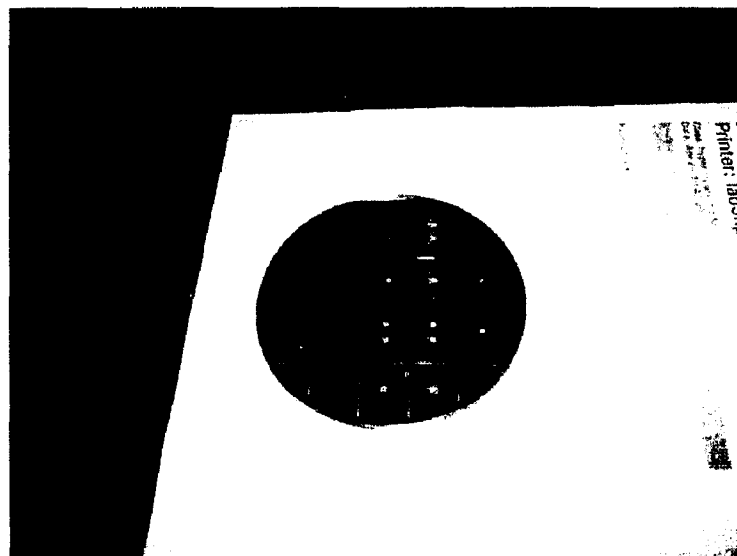

Figure 4.10 Assembled mold insert

The advantages of this method are that its process is simple and the steel plate will never be broken. The steel plate is reusable when the mold insert is worn out or broken. When the insert is heated up again to 350 °C, the glue will be carbonated and the silicon wafer can be removed so that the steel disk can be used for another mold insert again.

4.3 Hot embossing process

After the mold insert is formed, it will be mounted on the tool chucker, which is on the upper part of the vacuum chamber (Fig. 4.11).

Figure 4.11 Mold insert is mounted on the hot embossing system

The upper part of the vacuum chamber is connected with the force unit. In a hot embossing process, the PMMA sheet is placed on the substrate holder right below the mold insert. The substrate holder is on the lower part of the chamber. After the chamber is evacuated down below 1 mTorr, the mold and PMMA are heated above the glass transition temperature of the PMMA separately, but at the same time. Then the mold is embossed into the PMMA under a controlled force for a while. Still applying the embossing force, the tool and PMMA are cooled down just below the glass transition temperature. The mol insert is then demolded from polymer. The procedure is illustrated in Fig. 4.12.

a) A polymer sheet or is place in the chamber where a mold insert is installed.

b) Evacuate the chamber.

c) Lower the mold insert so that it just touches on the polymer sheet. Heat the

   mold insert and polymer separately in the same time above the glass transition

   temperature of the polymer so that ensures sufficient flow ability of the plastic

   material.

d) Press the mold insert into the polymer under a controlled force.

e) After filling the microcavities of the mold insert, the plastic material is cooled

   down to a temperature which provides for a sufficient strength. Then the

   microstructured plastic material can be demolded.

f) Open the chamber and take out the finished product.

The next process routine could be continued.
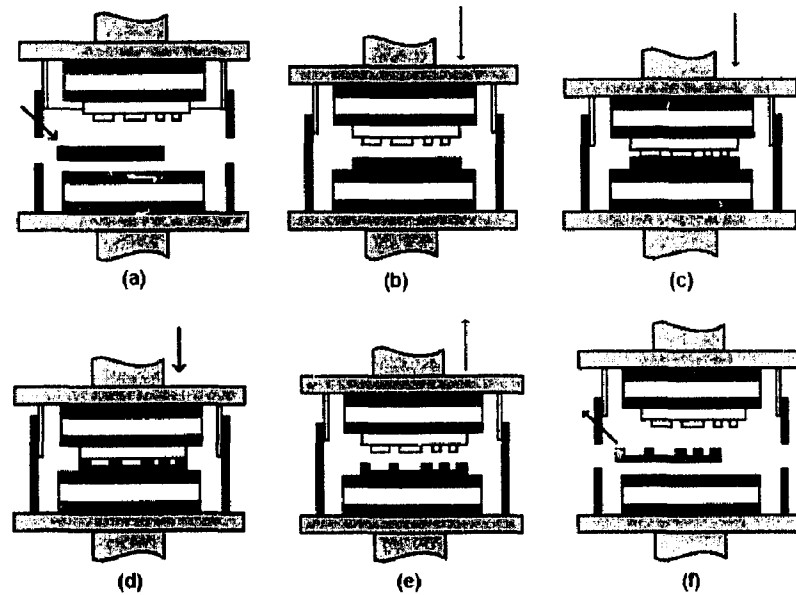
Figure 4.12 Sketch of the hot embossing procedure

Schematic view for embossed structure in detail is illustrated in Fig. 4.13.
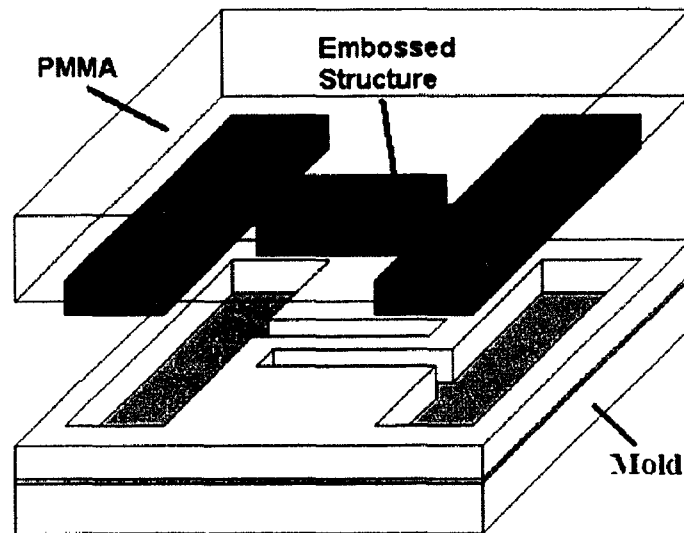
Figure 4.13 Sketch of an embossed structure with mold

The specific parameters for our process were as follows:

1. Evacuate the chamber to 1mTorr

2. Heat the mold and PMMA sheet both to about 135 °C

3. Insert the mold into PMMA sheet till the press force getting 35000N

4. Stay 5 minutes with above temperature and force

5. Cool mold and PMMA to 90°C

6. Demolding with speed of 1 μm/s

The whole processing cycle is about 20 minutes. The embossed PMMA sheet is shown in Fig. 4.14
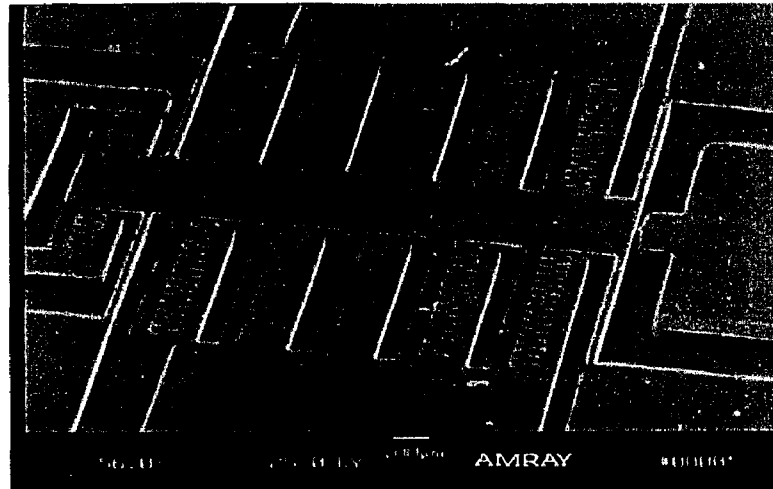
Figure 4.14 A good result on PMMA by hot embossing

4.4 Device assembly
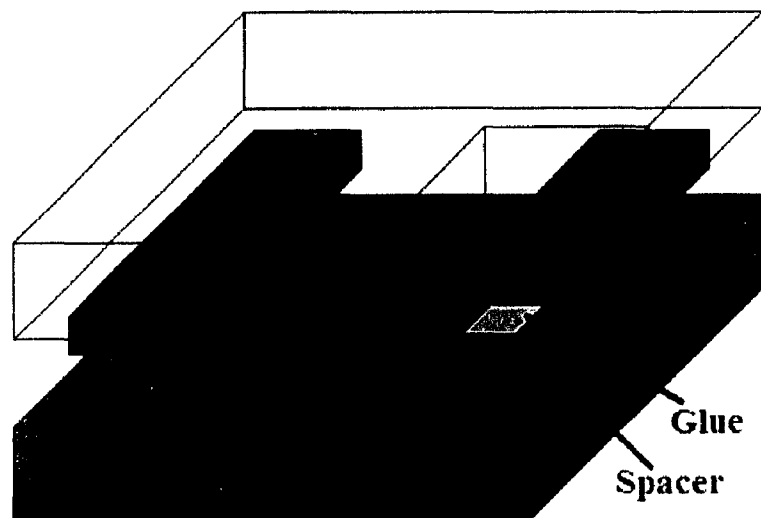
Figure 4.15 Embossed structure flipped glues on the spacer

In order to release the movable part, the second PMMA substrate with bonding pads was fabricated. The bonding pads also serve as spacers. The space height was about 100 μm. Then the substrate with comb drive structure was flipped upside down and bonded onto the second substrate with epoxy. The lateral size of the spacers on the lower substrate was made 200 μm smaller than that of bonding pads on upper structure

substrate purposely. In this way, the different parts will not be electrical connected by the followed metallization process. The whole processing is illustrated in Fig. 4.15.

The spacers can be formed either by drying etching or hot embossing. Hot embossing is preferred because it is simple and fast. A metal masking layer is needed for dry etching. Therefore, lithography, metal deposition, and strip-off processes are necessary every time in the dry etching method.

4.5 Movable part releasing and metallization

After the two substrates are bonded together, the next step is to release the movable part of the comb drive structure. To realize this, the PMMA backside in the strucutre substrate was etched all the way down to the comb drive structure. Because the total thickness was about 500 μm, fast removal of the PMMA is necessary. The PMMA was abraded with fine sand papers and polish films about 50 μm to the structure. An even thickness of 20 to 30 μm can be easily achieved using this abrading method because the PMMA is soft. Then the remaining PMMA was etched by Reactive Ion Etching (RIE) using gases of O_2 and SF_6. The etching rate is about 0.5 μm/min. This process step is illustrated in Fig. 4.16.
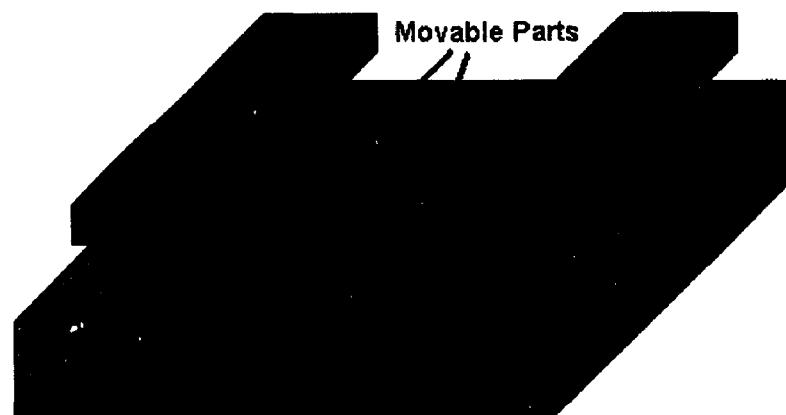

Figure 4.16 Structure after movable parts released

Metallization is done by sputtering Ti/Au = 1000Å/1000 Å after structure released.

Then wires are bonded on the electric pads using conductive epoxy. Now the device is

ready for testing. This last step is illustrated in Fig. 4.17
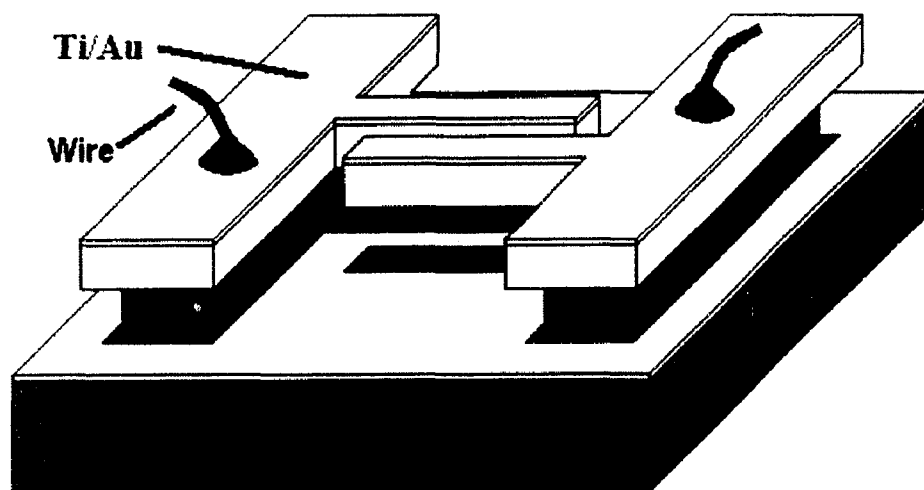


Figure 4.17 Structure after metallization and wire bonding

Fig. 4.18 shows 'ıe sketch of the whole structure and a real structure of the SEM

photo is shown in Fig. 4.19.
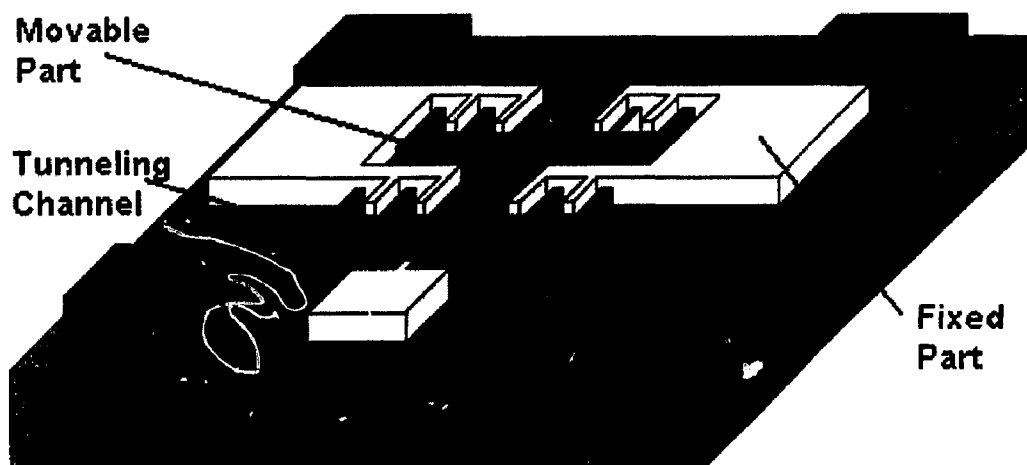
Figure 4.18 Sketch of the whole structure
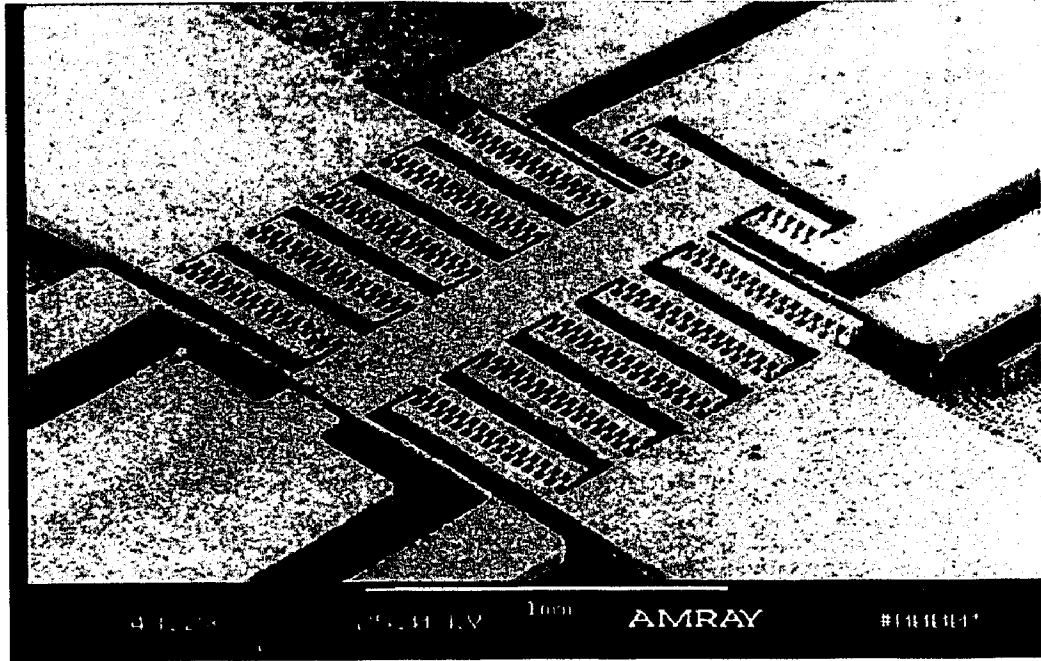
(a)
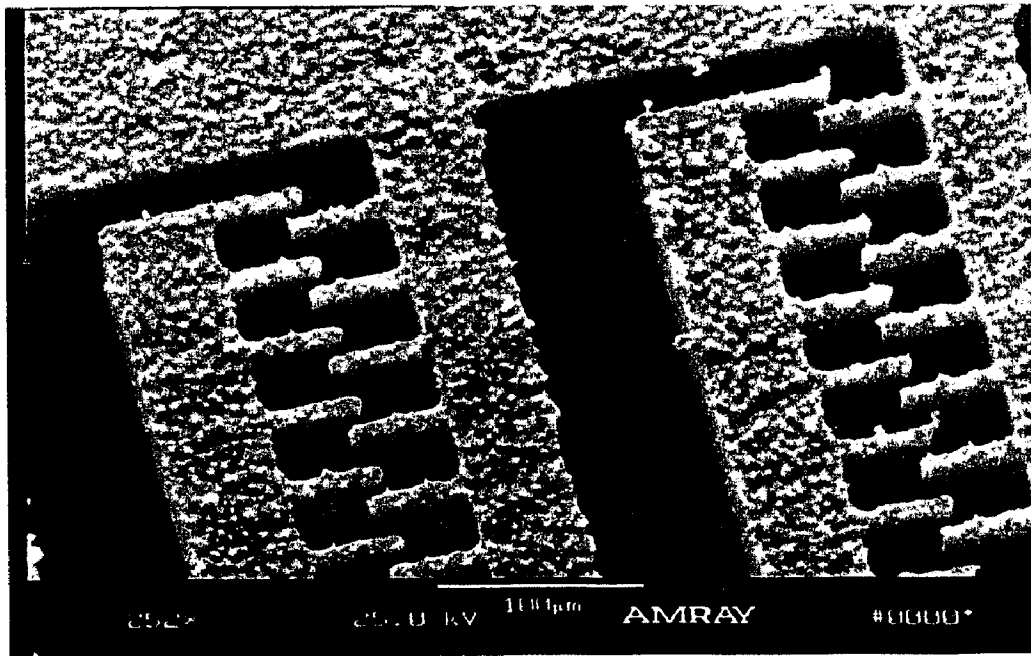
(b)

Figure 4.19 SEM photo of the final structure

CHAPTER FIVE

MEASUREMENTS AND DISCUSSION

5.1 Static Measurement

After wire bonding, the static measurement can be performed immediately. A high

voltage generator is connected to the fixed part of the comb drive. A small voltage is

applied on the movable fingers. The tip-electrode which is 5 μm away from the

suspension beam, is connected to the ground through a series resistor. The schematic

view of the configuration is shown in Fig. 5.1.
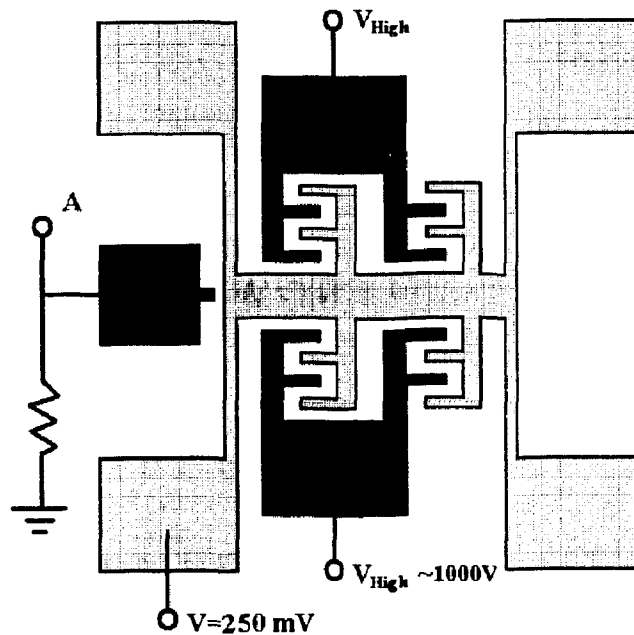
Figure 5.1   Measurement configuration

The device is put under a microscope with a CCD camera. When high voltage is applied on the comb drive, movement of the suspension beam toward to the tip can be clearly seen on a computer screen. A voltage of 250 mV is obtained at point A in Fig. 5.1 when the high voltage is increased to around 180 V, which indicates that the beam touches the tip-electrode. Thus, the final result is that the comb drive strikes 5 μm under 180 V potential because the initial distance from tip-electrode to the suspension beam is 5 μm.
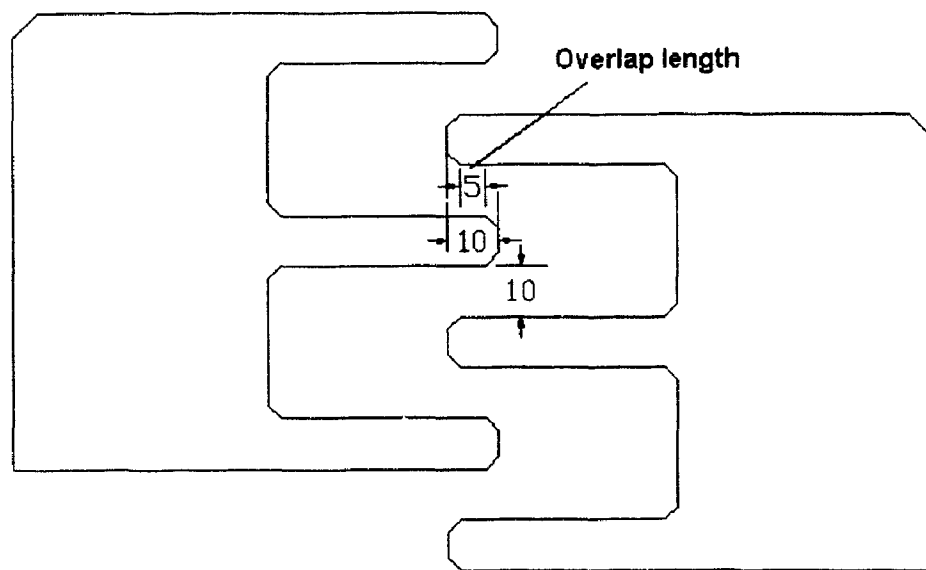
Figure 5.2 Overlap length of the fingers

It is found that the relationship between beam movement and applied voltage is not linear. There is little movement till applied voltage reaches 50 V. The beam moves obviously after 50 V. Then the movement enters the linear region. A mistake is found on design by double checking the mask layout. The initial overlap length of the fingers is only 5 um, which is too short. The minimum overlap length should be 20 μm according to the simulation result. Taking this factor into account, we can say that the real actuation

potential should be about 130 V for striking 5 um. This figure matches the designed value of 110 V well.

5.2 Dynamic Measurement

Dynamic measurement is used mainly to get the natural frequency in 1st mode. The measurement configuration is shown in Fig. 5.2.
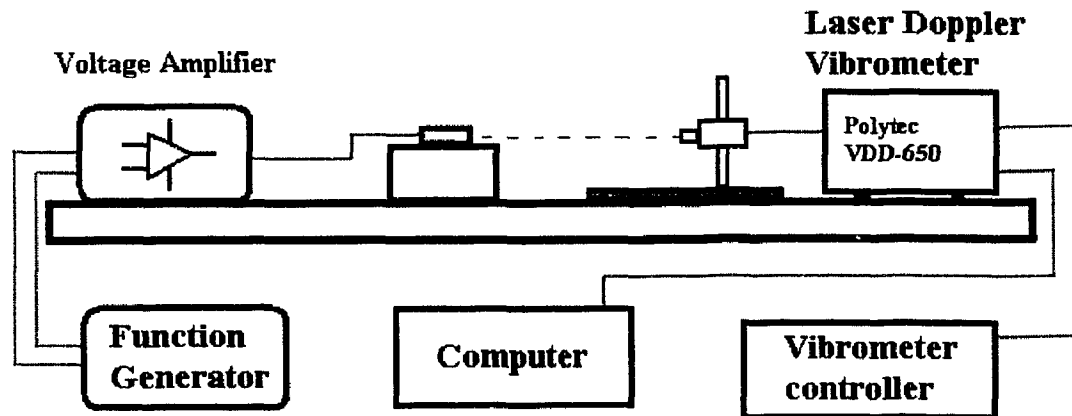
Figure 5.3   Dynamic measurement configuration

The comb drive is driven by a sine wave voltage signal. Because the maximum output voltage of the function generator is only ±10V, a self-made amplifier that has a maximum output voltage up to ±50V is added. The movement of the comb drive fingers is detected by a Digital Laser Doppler (LDV) vibrometry from Poly-tech Company.

LDV is a non-contact vibration measurement technique using the Doppler Effect. Laser vibrometers detect the phase difference between an internal reference and the measurement beam. The measurement beam is focused on the target and scattered back to the interferometer. The heterodyne principle used in Polytec vibrometers generates an FM carrier to provide the directional information, and also opens the possibility to digital traceable vibrometry.

Table 5.1 Vibration amplitudes at different driven frequency

Frequency (Hz)	Amplitude (um)	Frequency (Hz)	Amplitude (um)	Frequency (Hz)	Amplitude (um)
1	0.55	1600	0.80	3000	5.50
5	0.60	1700	0.85	3100	5.50
10	0.65	1800	0.80	3200	4.00
20	0.65	1900	0.85	3300	2.60
50	0.70	2000	0.90	3400	1.90
100	0.70	2100	1.00	3500	1.50
200	0.70	2200	1.05	3600	1.20
300	0.70	2300	1.20	3700	1.05
1000	0.75	2400	1.40	3800	0.90
1100	0.75	2500	1.50	3900	0.75
1200	0.75	2600	1.80	4000	0.65
1300	0.80	2700	2.20	4500	0.40
1400	0.75	2800	3.20	5000	0.20
1500	0.80	2900	4.50		

Displacement is electronically derived by measuring the phase change at the detector as the surface motion of the object changes the total path length of the beam. The displacement signal is monitored on a computer screen. The resolution of our LDV could reach 1Angstrom.
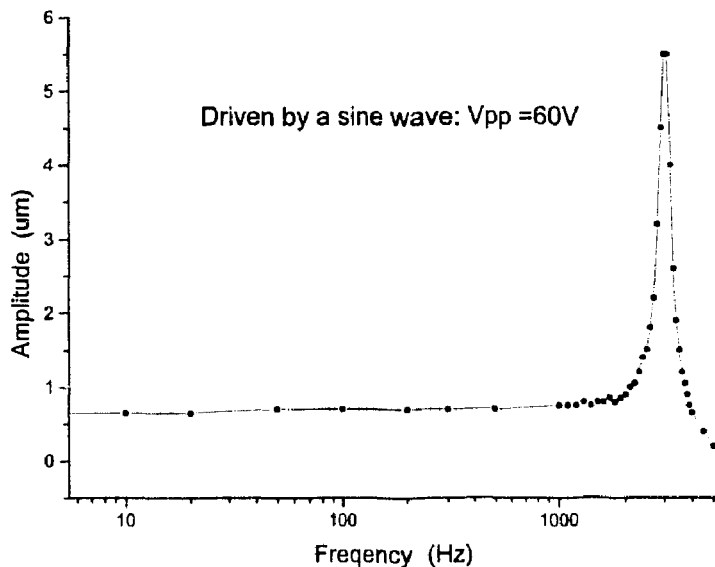
Figure 5.4   Vibration amplitudes vs driven frequency

The measurement was performed by fixing driven voltages with s ne wave with the Vpp=60 V. Then the vibration amplitudes at different frequency were recorded. The typical result is list in table 5.1 and the Fig. 5.3 shows the chart in logarithmic scale

From the table or chart, we can see that the measured natural frequency for 1st mode was around 3000 Hz. This value matches the simulation result very well.

CHAPTER SIX

CONCLUSIONS AND FUTURE WORK

6.1 Process Accomplishments

A lateral comb drive made of PMMA, using the hot embossing technique, has been realized.

Finite Element Analysis using ANSYS as an aided method in design was successfully employed. In the ANSYS simulation, static analysis, modal analysis and harmonic analysis were all performed to decide the key dimensions and structures. Electrostatic field analysis was also performed to decide the driving force. The final experimental results match the simulation results very well, which indicates that FEA simulation is a very good means to design a comb drive on PMMA.

Gluing a silicon wafer mold onto a stainless steel disk as a new method to form a mold insert has been developed. This method has several advantages such as

a) Simplicity: Only a hot plate is necessary. Complicated cleaning processes are not required.

b) Low cost: Materials (glue and stainless steel) are both very cheap. The stainless steel disk can be reused.

c) Ease of handling: The glue can be coated by hand, and the glue will be liquidized

at its cure temperature. Thus, the evenness and uniformity of the adhesion is

ensured when a proper weight is put on

A SOI wafer as a mold has been tried. With a SOI wafer mold, an even structure in

thickness with a very smooth surface has been obtained.

The problems of area dependent etching and micrograss in ICP etching process have

been solved by using a SOI wafer. The undercut problem in the ICP process has been

solved by using assistant thin walls, which ensures that the dimensions of open windows

are in the same range.

The hot embossing process for a comb drive structure with the minimum feature size

of 5 μm and aspect ratio of 12 has been developed.

Releasing movable structures on PMMA has been developed. The method that fixing

the structures onto a support substrate by means "Flip Chip" process and then removing

the back side PMMA to release the movable parts has been proven a successful process.

Using smaller spacers to separate the different parts electrically in metallization

process has been proven a simple yet successful process.

In addition, other processes such as fast removal of PMMA and PMMA etching by

RIE under low temperature have also been developed.

6.2 Advantages

Several advantages of the whole technique (forming a comb drive on PMMA using

hot embossing) are observed in this experiment as follows:

(1) The whole process is low cost and simple. First of all, the raw material of the PMMA is much cheaper than the traditional material of Silicon. The whole process only needs two hot embossing processes (20 minutes for one process), followed by bonding, thinning, and metallization.

(2) All the processes were performed under relatively low temperature, below 140°C; low temperature makes both the machine system and the process simpler.

(3) The PMMA structure has less stress and higher flexibility compared with the counterpart on silicon or poly-silicon. Less stress and higher flexibility make the device handling easier during fabrication processes.

(4) The driving voltage is also much lower compared with the silicon-based devices because PMMA has a lower Young's modulus. For the same structures and stroke distance, the necessary driving potential for a comb drive on PMMA is about 7 times less than one on silicon.

6.3 Future Work

Because this work is preliminary, there is much room for improvement in areas such as reducing the actuation potential, increasing the stroke distance and adjusting the natural frequency. For example, the distance between fingers is 10 μm, which could be easily reduced to 5 μm, according to our experience. Driving force is inversely proportional to the square of the actuation potential. Thus, in our structure if the finger gaps could be reduced to 5 μm from 10 μm, then the driving potential could be reduced from 130 V to 33 V for a 5 μm stroke. The current aspect ratio for the finger gap is 6:1. This value could be increased to some extent, too. Increasing the aspect ratio could reduce the drivng potential voltage.

For other future applications, this comb drive design could be used as a tunneling accelerometer. In order to show how the design could be used as a tunneling accelerometer, the schematic view of the structure is shown again in Fig. 6.1. According to quantum mechanics, an electron tunneling current occurs when two conductive electrodes approach each other within about 10 angstroms under a voltage potential. Tunneling current varies exponentially with the distance of the two electrodes. This exponential relationship between the tunneling current and the electrode distance enables tunneling accelerometers having extremely high resolution and sensitivity. For the conductive electrodes made of gold films, each Angstrom variation in distance can result in one order of magnitude changing in tunneling current. A simple circuit would be able to detect changes as small as 0.003Å. A tunneling accelerometer with a resolution of 20 ng/$\sqrt{Hz}$ and bandwidth of 5Hz - 1.5 KHz has been reported[31]
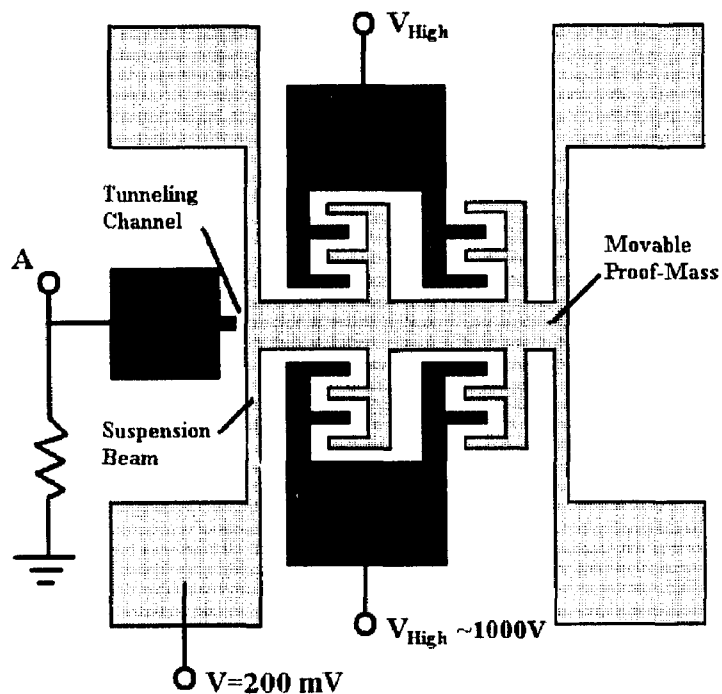

Figure 6.1   Design worked as a tunneling accelerometer

Another important advantage of tunneling sensors is that the tunneling current is not directly dependent on the dimension of the sensor. The tunneling occurs only between the two closest atoms. As a result, the tunneling sensor is not limited by the scaling law and can be made very small in size without loss of resolution.

In Fig. 6.1, the movable part of the comb drive is worked as a proof mass which can sense the applied acceleration. The suspension beam and fixed tip are worked as two conductive electrodes. When the suspension beam is pulled approaching to the fixed tip within 10 Angstroms by the comb drive under high voltage, the electron tunneling current occurs between the tip and suspension beam where a small voltage bias of 200 mV is applied. The applied acceleration causes the variation of the electrode distance, which in turn results in the exponential changing of the tunneling current. The detection of the acceleration is achieved by measuring the vibration of the tunneling current

REFERENCES

[1] http://mems.sandia.gov/scripts/images.asp

[2] W. C. Tang, T.H. Nguyen and R. T. Howe, "Laterally Driven Polysilicon Resonant Micro-strutures," *in Tech. Dig. IEEE Micro Electro Mech. Syst. Workshop, Salt Lake City, UT, Feb.* 20-22, 1989, pp. 53-59.

[3] W. C. Tang, "Electrostatic comb drive for resonant sensor and actuator application," Ph. D. dissertation, Univ. California, Berkeley, CA, 1990.

[4] Johnson and Larry K. Warn, "Electrophysics of Micromechanical Comb Actuators," *Journal of Microelectromechanical Systems,* vol. 4, 1995, pp. 49-59

[5] Wenjing Ye, Subrata Mukherjee, and Norl C. MacDonald, "Optimal Shape Design of an Electrostatic Comb Drive in Microelectromecha-nical Systems," *Journal of Microelectromecha-nical Systems,* vol. 7, 1998, pp. 16-26

[6] M. Steven Rodgers, Sridhar Kota, et al. "A New Class of High Force, Low-Voltage, Compliant Actuation Systems," *www.mems.sandia.gov*

[7] J. L. Andrew Yrh, Chung-Yuen Hui and Norman C. Tien, "Electrostatic Model for an Asymmetric Combdrive," *Journal of Microelectromechanical Systems,* vol. 9, 2000, pp. 16-26.

[8] Toshiki Hirano, Tomotake Furuhata, Kaigham J. Gabriel and Hiroyuki Fujita, "Design, Fabrication, and Operation of Submicron Gap Comb-Drive Microactuators," *Journal of Microelectromechanical Systems,* vol. 1, 1992, pp. 52-59

[9] Pamela R. Patterson, et al, "A Scanning Micromirror with Angular Comb Drive actuation," *15th IEEE International Conference on MicroElectroMechanical Systems,* 2002, pp. 544-547.

[10] *http://www.jo-mikrotechnik.com*

[11] Roos, N., et al, "Nanoimprint lithography with a commercial 4 inch bond system for hot embossing," Proceedings of SPIE - The International Society for Optical Engineering, v 4343, 2001, pp 427-435.

[12] Heyderman, L.J., et al, "Nanofabrication using hot embossing lithography and electro-forming," *Microelectronic Engineering*, v 57-58, September , 2001, pp 375-380.

[13] Scheer, H.-C, et al, "Strategies for wafer-scale hot embossing lithography," *Proceedings of SPIE - The International Society for Optical Engineering*, v 4349, 2001, pp 86-89.

[14] Lee, G.-B, et al, "Microfabricated plastic chips by hot embossing methods and their applications for DNA separation and detection," *Sensors and Actuators, B: Chemical*, v 75, n 1-2, Apr 30 2001, 2001, p 142-148.

[15] Becker, H., at al, "Microfluidic devices for μ-TAS applications fabricated by polymer hot embossing," *Proceedings of SPIE - The International Society for Optical Engineering*, v 3515, 1998, pp 177-182.

[16] Holger Becker, Ulf Heim, "Hot embossing as a method for the fabrication of polymer high aspect ratio structures," *Sensors and Actuators, A: Physical*, v83, n1, 2000, pp. 130-135.

[17] Holger Becker, Ulf Heim, "Silicon as tool material for polymer hot embossing" *Proceeding MEMS 99*, 1999, pp. 228-231.

[18] K. –D. muller, et al, "3D Diced Microcomponents Fabricated by Multi-layer Hot Embossing. *ME'99 : Micromechanics Europe*, Gif-sur-Yvette, F, September 27-28, 1999.

[19] Roetting, Oliver, et al, "Production of movable metallic microstructures by aligned hot embossing and reactive ion etching," Proceedings of SPIE - The International Society for Optical Engineering, v 3680, pp. 1038-1045.

[20] Liwei, Lin, et al, "Microfabrication using silicon mold inserts and hot embossing," *Proceedings of the International Symposium on Micro Machine and Human Science*, 1996, pp. 67-71.

[21] http://www.engin.brown.edu/courses/en4/notes/Forcedvibes/Forcedvibes.html

[22] Hirano, Toshiki; et al., "Design, fabrication, and operation of submicron gap comb-drive microactuators," *Journal of Microelectromechanical Systems*, v 1, n 1, Mar, 1992, p 52-59.

[23] J.B. Starr, "Squeeze-film damping in solid-state accelerometers," *In Technical Digest, IEEE Solid State Sensor and Actuator Workshop, Hilton Head Island, South Carolina*, June 1990, pp. 44-47.

[24] Young-Ho Cho, et al. "Viscous Damping Model for Laterally Oscillating Microstructures" *Journal of Microelectromechanical System*, Vol. 3, No. 2, June 1994, pp. 81-86.

[25] ANSYS 5.7.1 on line documentation, Chapter 2. Structural Static Analysis

[26] ANSYS 5.7.1 on line documentation, Chapter 15. p-Method Electrostatic Analysis.

[27] Petersen, K.E., Silicon as a Mechanical Material, *Proceedings of the IEEE*, May 1982, Vol. 70, No. 5, pp.420-457.

[28] Holger Becker, et al, "Silicon as tool material for polymer hot embossing," *Proceedings MEMS'99*, Orlando 1999, 228-231.

[29] Henri Jansen, et el, "The black silicon method VI: High aspect ratio trench etching for MEMS applications," *The 9th annual international workshop on MEMS, IEEE, 1996*, p 250-257.

[30] A.A.Ayon, et el, "Characterization of a time multiplexed inductively coupled plasma etcher." *Journal of the electrochemical society*, 146 (1), 1999, p 339-349.

[31] Cheng-Hsien Liu and Tomas W. Kenny, "A High-Precision, Wide-Bandwidth Micro-machined Tunneling Accelerometer," Journal of Microelectromechanical Systems, vol. 10, 2001, pp. 425-433